

UC Berkeley

UC Berkeley Electronic Theses and Dissertations

Title

Mechanical Damage from Cavitation in High Intensity Focused Ultrasound Accelerated Thrombolysis

Permalink

<https://escholarship.org/uc/item/031704k7>

Author

Weiss, Hope

Publication Date

2012

Peer reviewed|Thesis/dissertation

**Mechanical Damage from Cavitation in High Intensity Focused Ultrasound
Accelerated Thrombolysis**

by

Hope Leigh Weiss

A dissertation submitted in partial satisfaction of the
requirements for the degree of
Doctor of Philosophy

in

Engineering - Mechanical Engineering

in the

Graduate Division

of the

University of California, Berkeley

Committee in charge:

Professor Andrew J. Szeri, Chair
Professor J. Karl Hedrick
Professor James Sethian

Fall 2012

**Mechanical Damage from Cavitation in High Intensity Focused Ultrasound
Accelerated Thrombolysis**

Copyright 2012
by
Hope Leigh Weiss

Abstract

Mechanical Damage from Cavitation in High Intensity Focused Ultrasound Accelerated
Thrombolysis

by

Hope Leigh Weiss

Doctor of Philosophy in Engineering - Mechanical Engineering

University of California, Berkeley

Professor Andrew J. Szeri, Chair

Stroke is the fourth most common cause of death in the United States (second worldwide), with about 87% of these being ischemic. Recent studies, *in vitro* and *in vivo*, have shown that High Intensity Focused Ultrasound (HIFU) accelerates thrombolysis, the dissolution of blood clots, for ischemic stroke. Although the mechanisms are not fully understood, cavitation is thought to play an important role in sonothrombolysis. Acoustic cavitation is typically divided into two categories describing the bubble behavior: stable cavitation describes bubbles undergoing smooth oscillations, while inertial cavitation is characterized by rapid growth followed by violent collapses. Possible mechanisms associated with both stable cavitation (i.e. microstreaming) and inertial cavitation (i.e. microjets) are thought to increase clot lysis by enhancing the delivery of a thrombolytic agent.

The damage to a blood clot's fibrin fiber network from bubble collapses in a HIFU field is studied. The bubble dynamical model used is the Keller-Miksis equation with a linear Kelvin-Voigt viscoelastic material to account for the clot material outside the bubble. The amount of damage to the fiber network caused by a single bubble collapse is estimated by two independent approaches. The first method is based on the stretch of individual fibrin fibers of the blood clot, and estimates the number of broken fibers as a bubble embedded in the blood clot grows to its maximum radius. This method estimates that fibrin fibers (the structural matrix of the blood clot) break as the bubble expands, however the bubble dynamical model does not account for this. To account for the breaking of fibrin fibers (and lysing of red blood cells) a term could be added to the Keller-Miksis equation. This motivates the second method, an independent energy based approach. In this method, the equation for the bubble dynamics, as the bubble grows to its maximum radius, is analyzed in the form of a work-energy statement. The energy method is extended to the more important scenario of a bubble outside a blood clot that collapses asymmetrically creating a jet towards the clot. There is significantly more damage from a bubble growing outside the clot compared to a bubble embedded within the clot structure.

Next, the effects of the physical properties of skull bone when a HIFU wave propagates through it are examined. The dynamics of a test bubble placed at the focus is used in understanding of the pressure field. The sound emitted from the bubble is used to classify the type of cavitation present (stable and/or inertial). The amount of damage in the area surrounding the focus is examined for various initial bubble sizes. The maximum amount of energy available to cause damage to a blood clot increases as the density of the calvaria decreases.

This dissertation is a first step in analyzing potential cavitation mechanisms, which have only been suggested by other authors. The goal is to assess the plausibility of mechanical damage as a mechanism for enhancement of sonothrombolysis with the addition of microbubbles. The methods to estimate mechanical damage derived here offer the first connection between a bubble and the damage it may cause to a blood clot. This work shows that a bubble near but exterior to a blood clot has the potential to cause significant damage. Ultimately, this dissertation contributes to the understanding of how microbubbles can accelerate clot destruction. This understanding will lead to improved design of therapeutic devices.

To the ones I love.

The poster is a vertical rectangular graphic with a light beige background. It is divided into four horizontal sections, each representing a letter of the word 'FAST'.
1. **F**ace: On the left, a large red 'F' is followed by the word 'ace' in black. To the right is a cartoon illustration of a man's face. Text next to it asks, 'Does the face look uneven? Ask them to smile.'
2. **A**rm: On the left, a large red 'A' is followed by 'rm' in black. To the right is a cartoon illustration of an elderly woman raising her right arm. Text next to it asks, 'Does one arm drift down? Ask them to raise both arms.'
3. **S**peech: On the left, a large red 'S' is followed by 'peech' in black. To the right is a cartoon illustration of an elderly woman speaking. A speech bubble above her says 'Bof fri fleu.' Text next to it asks, 'Does their speech sound strange? Ask them to repeat a phrase.'
4. **T**ime: On the left, a large red 'T' is followed by 'ime' in black. To the right is a cartoon illustration of a hand holding a mobile phone, a clock, and an ambulance. Text next to it says, 'Every second brain cells die. Call 9-1-1 at any sign of stroke!'
On the right side of the poster, there is a vertical column of text: 'Is it a stroke? Check these signs FAST!' in large, bold letters. Below this, it says 'Call 9-1-1 at any sign of stroke.' in a smaller font. At the top right, there is a small graphic of a 'STROKE HEROES ACT FAST' sign with icons for Face, Arm, Speech, and Time, and a mobile phone icon.

Face Does the face look uneven? Ask them to smile.

Arm Does one arm drift down? Ask them to raise both arms.

Speech Bof fri fleu. Does their speech sound strange? Ask them to repeat a phrase.

Time Every second brain cells die. Call 9-1-1 at any sign of stroke!

Is it a stroke? Check these signs **FAST!**

Call 9-1-1 at any sign of stroke.

Massachusetts Department of Public Health — For more information call 1-800-487-1119 or email heart.stroke@state.ma.us

Stroke Heroes Act FAST!

Image taken from the Memorial Hospital of Rhode Island

Contents

List of Figures	iv
List of Tables	vii
1 Introduction	1
1.1 Stroke	1
1.1.1 Types of stroke	1
1.1.2 Warning signs	2
1.1.3 Treatment	3
1.2 Sonothrombolysis	4
1.2.1 Ultrasound field characterization	4
1.2.2 Previous studies	5
1.2.3 Acoustic cavitation mechanisms	6
1.2.4 Hemorrhagic stroke	8
1.2.5 Assessing mechanical damage	8
1.3 Bubble dynamics	8
1.3.1 Keller-Miksis Equation	8
1.3.2 Sound emission	10
1.4 Summary of original contributions	10
2 Mechanical Damage to a Blood Clot from Bubble Dynamics	12
2.1 Introduction	12
2.2 Materials and Methods	13
2.2.1 Clot Model	13
2.2.1.1 Testing Tube	13
2.2.2 Experimental Setup	14
2.2.3 Acoustic Field Characterization / Passive Cavitation Detection	14
2.3 Experimental Images	15
2.3.1 Scanning Electron Microscopy	15
2.3.2 Acoustic Field	18
2.3.3 Motivation for Mechanical Damage	18

2.4	Theoretical and Numerical Methods and Results	19
2.4.1	Clot Properties	19
2.4.2	Bubble Dynamics	20
2.4.3	Strain Method for Estimation of Cavitation Damage for an Embedded Bubble	21
2.4.4	Work Method for Estimation of Cavitation Damage for an Embedded Bubble	28
2.4.5	Work Method for Estimation of Cavitation Damage for an External Bubble	33
2.4.6	Pressure field design	37
2.5	Discussion and Conclusions	38
3	Effects of Skull Properties on Cavitation	40
3.1	Introduction	40
3.2	HIFU Model	41
3.3	Cavitation Model	42
3.3.1	Bubble Dynamics	42
3.3.2	Sound Emission	43
3.3.3	Connection to Mechanical Damage	43
3.4	Results	43
3.4.1	Pressure Distribution	43
3.4.2	Effects of Skull Density on Dynamics of a Test Bubble	46
3.4.3	Power Spectrum of Emitted Sound	48
3.4.4	Connection to Mechanical Damage	51
3.5	Conclusion	55
4	Discussion	56
4.1	Summary of contributions	56
4.2	Future work	58
	Bibliography	60
A	Geometric derivation for strain	67

List of Figures

1.1	Types of Strokes (Image taken from the Centers for Disease Control and Prevention [1].)	2
1.2	The radial responses of a bubble (R_0 fixed) over time for various amplitudes of the applied pressure wave (sinusoidal). The bubble goes from stable to inertial cavitation as the pressure amplitude is increased.	7
1.3	The conceptual representation of a Kelvin-Voigt material where G and μ are the shear modulus and viscosity of the viscoelastic material, respectively.	9
2.1	Thrombus on a silk thread. Figure courtesy of T. Hoelscher.	14
2.2	Top view inside the tank, showing inlet/outlet, test tube, transducer positioned above and PCD hydrophone positioned aside. Figure courtesy of T. Hoelscher.	15
2.3	Scanning Electron Micrograph of a human citrate blood clot before HIFU treatment (left column) and after HIFU treatment (right column). The image shows a dense fibrin fiber network with numerous cells incorporated into the matrix. (Figure courtesy of G. Ahadi, Hoelscher group, UCSD.)	17
2.4	Spectrum plots for sonications below (800 kPa , black) and above (4.3 MPa , green) the cavitation threshold. Green plots exhibits sub & ultra harmonics (stable cavitation) and also broadband signal elevation (inertial cavitation). Lower plot was used as a baseline reference to calculate cavitation activities. (Figure courtesy of A. Voie, Hoelscher group, UCSD.)	18
2.5	Dynamics of a single bubble wholly embedded in a blood clot, for various acoustic input amplitudes, $P_A = 0.5, 1.0, \text{ and } 1.5 \text{ MPa}$ for a bubble with initial radius $R_0 = 1 \text{ }\mu\text{m}$.	21
2.6	Sketch of the deformation. The bubble expands from R_0 in the reference configuration, to $R(t)$ in the deformed configuration. Accompanying this is a deformation of the surrounding clot matrix. In particular, an individual fibrin fiber aligned closely with \mathbf{e}_r in the reference configuration is deformed to lie more closely to \mathbf{e}_θ and stretched when $R(t) > R_0$.	22

2.7	The number and fraction of broken fibers for the bubble dynamics shown in Fig. 2.5. (a) Estimates of the number of broken fibers in a shell of thickness $dr = 0.1 \mu m$, plotted as a function of the distance from the bubble center in the reference configuration. (b) The fraction of broken fibers is also shown as a function of distance from bubble center. As expected, the highest fraction of fibers broken are close to the initial bubble surface.	27
2.8	The bubble dynamics for a bubble in blood and the dynamics for a bubble wholly embedded in a blood clot, assuming no damage occurs during growth are plotted for $R_0 = 1 \mu m$ and $P_A = 1.5 MPa$. These provide an upper and lower bound, respectively, for the expected bubble dynamics, accounting for damage to the blood clot, for a bubble wholly embedded in a clot.	31
2.9	A $1 \mu m$ bubble in blood subjected to a $0.5 MPa$ acoustic wave. These plots show the relationship in time between R , \dot{R} , $P_A \sin(\omega t)$, the bubble volume and W_{AC}	36
2.10	The maximum amount of energy available in nJ for breaking fibers from an external bubble is plotted for various initial radii (R_0) and various applied pressure amplitudes (P_A).	37
3.1	Experimental setup: (1) Needle hydrophone for passive cavitation detection system, (2) Flow inlet, (3) Data analysis, (4) Microbubble infusion, (5) Unidirectional flow pump, (6) Hemispherical, helmet transducer filled with deionized, degassed water, (7) Human calvaria mounted on an acrylic fixture, and (8) Human blood clot.	42
3.2	Temporal variation of the pressure at the focus for a lower, median and higher density skulls.	45
3.3	Radial dynamics of a bubble in water with initial radius of $0.27 \mu m$ in the left column and $8.0 \mu m$ in the right column located at the focus for a lower, median and higher density skulls.	47
3.4	Convergence of the power spectrum for a bubble in water with initial radius of $1 \mu m$ for $(-)$ $N = 10^3$, $(-)$ $N = 10^4$, $(-)$ $N = 10^5$, and $(-)$ $N = 10^6$. As the length, N , of the sound signal is increased, the resolution of the FFT increases. Suitable convergence is found.	48
3.5	Acoustic power spectrum of a bubble in water with an initial radius of $0.27 \mu m$ in the left column and $8.0 \mu m$ in the right column located at the focus for a lower, median and higher density skulls.	50
3.6	The maximum radii in μm (left) and amount of energy available to break fibers and red bloods cells in nJ (right) along each axis as the initial bubble radius is varied for a calvaria of LOWER density. The focus is located at $0 mm$ on each axis.	52

3.7	The maximum radii in μm (left) and amount of energy available to break fibers and red bloods cells in nJ (right) along each axis as the initial bubble radius is varied for a calvaria of MEDIAN density. The focus is located at 0 mm on each axis.	53
3.8	The maximum radii in μm (left) and amount of energy available to break fibers and red bloods cells in nJ (right) along each axis as the initial bubble radius is varied for a calvaria of HIGHER density. The focus is located at 0 mm on each axis.	54

List of Tables

2.1	The total number of fibers broken and the energy used breaking them for various applied acoustic magnitudes.	28
2.2	The work done on the bubble by the acoustic wave, the potential energy of the gas, the work done by surface tension, the stored energy in the fluid and the viscous loss to the fluid for a $R_0 = 1\mu m$ bubble for $P_A = 1.5 MPa$	32
2.3	The work done by the acoustic wave, the work done by the gas pressure, the work done by surface tension, the stored energy in the fluid and the viscous loss in the fluid for a bubble embedded in a clot with no damage and a bubble in blood for a $R_0 = 1\mu m$ bubble for various applied acoustic pressure magnitudes. The maximum number of broken fibers is computed using the upper bound from Eqn. 2.23 divided by the energy to break a single fibrin fiber.	33
2.4	The amount of work done by the acoustic wave on the bubble until collapse, W_{AC} , is transferred to the kinetic energy of the jet. This provides an upper bound for the number of fibers broken.	34
3.1	Peak positive and peak negative pressure at the focus for median density, lower density and higher density skulls.	44

Acknowledgments

First and foremost, I want to thank my advisor, Andrew Szeri, for the support, patience, and guidance given to me over the past 6 years here at Berkeley. Andrew, I look forward to advising my future students and passing on the knowledge I have learned from you. Thanks also to the other members of my dissertation committee, Karl Hedrick and James Sethian and to my valued collaborators at the University of California, San Diego, Thilo Hoelscher, Golnaz Ahadi, and Arnie Voie. Many thanks to the Mechanical Engineering department staff for all the help throughout the years.

The work presented in this dissertation was funded partially through a National Science Foundation Graduate Research Fellowship. Funding was also provided by three Graduate Division Block Grant Awards, funding from the University of California at Berkeley-King Abdullah University of Science and Technology Academic Excellence Alliance, and an awesome Graduate Student Instructor position for CE 100 with Evan Variano.

To the ones who keep me sane, I thank you. I am glad to have shared some of my life, great discussions, and knowledge with these wonderful people, my lab mates (and friends): Beth, Vera, Jean, Prashanth, Savas, Stephane and Su Chan. Also, those friends very important to me who have been there over the years, I recognize what you have dealt with and words cannot describe how much you all mean to me: Statia, Jon, Christine, Johanna, Sarah, Lindsay, and Jacob. And to all my softball teammates current and past, good luck!

Lastly, to my family thank you for all the support and the endless questions about when my work would be done. Here it is, enjoy.

Chapter 1

Introduction

1.1 Stroke

The World Health Organization lists stroke as the number two cause of death worldwide, with an estimated 6.15 million deaths per year [2]. In the United States, stroke is the number four cause of death, killing more than 137,000 people a year (approximately 1 in every 18 deaths) in 2008 [3]. In the United States, stroke is a leading cause of long-term disability and the direct and indirect cost of stroke was \$73.7 billion in 2010.

1.1.1 Types of stroke

A stroke, also sometimes called a “brain attack”, happens when there is a disturbance in the blood flow to a part of the brain. This can happen when the bloody supply to part of the brain is interrupted or severely reduced, known as an ischemic stroke, or when a blood vessel in the brain bursts, known as a hemorrhagic stroke. With both types of stroke, there is a lack of oxygen to the affected part of the brain, which within minutes can lead to brain cells dying and brain damage.

Ischemic stroke occurs when there is a partial or full occlusion of the blood vessel supplying blood to the brain, see Fig. 1.1. It accounts for around 87% of all strokes. Ischemic strokes can occur in two ways: thrombotic or embolic strokes. In a thrombotic stroke, the blood flow is obstructed, by a thrombus (blood clot) that develops in the blood vessel, in one or more of the arteries supplying blood to the brain. An embolic stroke occurs when a blood clot forms elsewhere in the body, usually the heart, and a part of that clot breaks off and travels through the bloodstream to the brain. In the brain, the clot will travel until it reaches a blood vessel small enough to deny it passage. Now trapped, the clot blocks the blood vessel causing a stroke. A blood clot consists of a structural matrix of fibrin fibers with entrapped platelets and red blood cells.

The remaining roughly 13% of strokes are hemorrhagic strokes. A hemorrhagic stroke occurs when a weakened vessel ruptures, causing blood to leak into the brain, see Fig. 1.1.

There are two types of hemorrhagic strokes: intracerebral and subarachnoid hemorrhages. An intracerebral hemorrhage is caused when a burst blood vessel bleeds into the brain. High blood pressure is the primary cause of this type of stroke. In a subarachnoid hemorrhage, a blood vessel bursts near the surface of the brain causing blood to fill into the area around the outside of the brain. The most common cause of this type of stroke is a ruptured aneurysm.

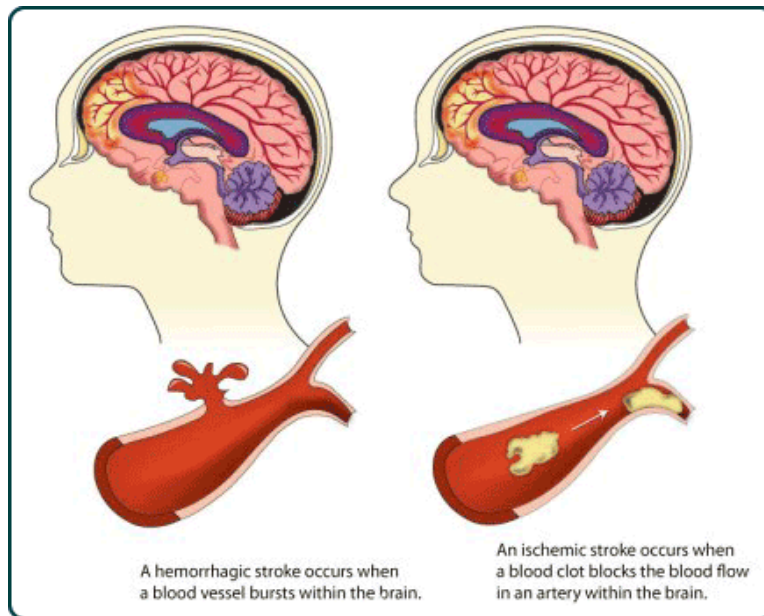


Figure 1.1: Types of Strokes (Image taken from the Centers for Disease Control and Prevention [1].)

1.1.2 Warning signs

The warning signs for stroke are

- Sudden numbness or weakness of the face, arm or leg, especially on one side of the body
- Sudden confusion, trouble speaking or understanding
- Sudden trouble seeing in one or both eyes
- Sudden trouble walking, dizziness, loss of balance or coordination
- Sudden, severe headache with no known cause

If you or someone you are with has one or more of the aforementioned symptoms, call 9-1-1 immediately.

Studies from around the world have shown poor awareness for the risk factors and warning signs of stroke [4, 5, 6, 7, 8]. This knowledge is essential for the prevention and immediate treatment of stroke. Kothari et al. [4] conducted a study of patients in the US admitted to the emergency room with a diagnosis of stroke to determine their knowledge of the signs, symptoms, and risk factors for stroke and heart disease. Their results showed that almost 40% of patients admitted with a possible stroke did not know a single sign or symptom of stroke. The study by Das et al. [5] in India, interviewed not only stroke patients but healthy people who accompanied the patients. They found a significant association with the level of knowledge of stroke warning symptoms and the education level of the person for both groups. The study also looked at the source of information for these groups and found that doctors/health workers and the government provided little health education on strokes. In Australia, where stroke is the third most common cause of death, Sug Yoon et al. [6] assessed the knowledge of the general urban population through a telephone interview. In this study, almost 73% of respondents listed more than one risk factor for stroke and nearly 50% of respondents listed more than one warning symptom. A study in Ireland by Hickey et al. [7], looked at the awareness of older adults. When given a list of warning signs, they found that only one warning sign (slurred speech) was identified by more than half (54%) of the respondents. The conclusion from all of these studies is to provide more education to improve the general populations knowledge and awareness of stroke.

1.1.3 Treatment

The course of treatment for a stroke is dependent on the type of stroke the patient is having. For hemorrhagic stroke treatment, the focus is on controlling the bleeding, reducing pressure on the brain and stabilizing vital signs, especially blood pressure. For an intracerebral hemorrhage, the treatment protocol is determined based on a computerized tomography (CT) scan of the patients brain and can consist of medications and/or surgery. For a subarachnoid hemorrhage, surgical treatment is often recommended. The types of surgery used include, surgical clipping (a clip is placed at the base of the aneurysm) and coiling (a catheter is used to introduce a coil into the aneurysm, thus reducing or blocking the flow of blood to the aneurysm).

Treatment for ischemic stroke focuses on restoring the flow of blood to the brain and can include medicine and medical procedures. Several types of medications are typical treatment for ischemic strokes and include antiplatelets (inhibits aggregation of platelets to reduce the likelihood of another stroke), anticoagulants (“blood thinners,” also reduce the risk of a secondary stroke) and thrombolytics (break up the blood clot). The only drug approved for ischemic stroke treat by Federal Food and Drug Administration (FDA) is recombinant tissue plasminogen activator (rt-PA). rt-PA, which binds to the fibrin in the blood clot, works by activating plasminogen, which also binds to the fibrin of the blood clot, and forms plasmin. Plasmin then digests the fibrin, dissolving the framework of the blood clot. Current FDA guidelines state that rt-PA can only be given within the first three hours of the onset of the

stroke, which is why it is critical to be aware of stroke warning symptoms. Recently, it was recommended that the time requirement be extended from 3 hours to 4.5 hours [9], but it has not been FDA approved yet. It is estimated that only 1-5% of all ischemic stroke patients taken to emergency rooms are administered rt-PA [10, 11]. The drug can be administered intravenously or by an arterial catheter.

Two catheter-based medical systems with FDA approval for treatment of ischemic stroke are the MERCI retrieval system and the Penumbra system. The MERCI system uses a corkscrew-shaped device, which wraps around the clot, entrapping it. The clot is then removed from the body. This system has a treatment window of 8 hours and can be safely used after the 3 hour window for rt-PA administration has expired. The Penumbra system works by dislodging the clot, then using a suction device removes the blood clot. This system can be used within an eight hour window after the onset of the stroke.

1.2 Sonothrombolysis

New medical treatments to salvage ischemic tissue that are less restrictive (by increasing the treatment window) and/or more efficient are needed. A new emerging treatment for both ischemic and hemorrhagic stroke is therapeutic ultrasound.

1.2.1 Ultrasound field characterization

Before reviewing the studies on sonothrombolysis, it is important to have an understanding of ultrasound field characteristics. A continuous ultrasound wave is sufficiently described by frequency, period, wavelength and propagation. Several more terms need to be included for pulsed wave ultrasound, including duty cycle (the fraction of time the ultrasound wave is generated), pulse length (time length of a single pulse), and pulse repetition frequency (number of pulses per second). Measures of how strong or intense the ultrasound wave is are needed. The pressure amplitude is usually described by the peak positive and peak negative pressures. The acoustic power (the amount of acoustic energy generated per unit time) of the ultrasound wave is dependent on many of these characteristics. Intensity is the rate at which energy flows through a unit area and is important when discussing bioeffects. For pulsed wave ultrasound there are six intensities of importance:

- Spatial average-temporal average (SATA)
- Spatial peak-temporal average (SPTA)
- Spatial average-pulse average (SAPA)
- Spatial peak-pulse average (SPPA)
- Spatial average-temporal peak (SATP)

- Spatial peak-temporal peak (SPTP)

where the temporal average (TA) is the measured average over the entire pulse repetition period (1/pulse repetition frequency), the pulse average (PA) is the measured average for a given pulse duration, the temporal peak (TP) is measured when the pulse is present (no averaging), the spatial peak (SP) is the maximum intensity at a specific location and the spatial average (SA) is the spatial-average intensity. The highest intensity is SPTP (since it is not an average) and the lowest intensity is SATA (since it averages in space and time.) The most commonly reported intensity is SPTA.

The Mechanical Index (MI) is used as an indicator of the likelihood of mechanical bio-effects, including cavitation. The MI was originally derived as an indicator for transient cavitation for short pulse, low duty cycle ultrasound [?]. It is defined as the peak negative pressure divided by the square root of the ultrasound frequency.

1.2.2 Previous studies

Ultrasound has been shown *in vitro* [12, 13, 14, 15, 16, 17, 18, 19, 20, 21] and *in vivo* [22, 23, 24, 25, 26, 27, 28, 29, 30, 31, 32] to accelerate thrombolysis. The majority of these studies include rt-PA or other fibrinolytic chemicals.

In 2006, Frenkel et al. [18] evaluated the impact of high intensity focused ultrasound (HIFU) (1 MHz; 10% duty cycle; total acoustic power, 60 W) with and without rt-PA in an *in vitro* human blood clot model. No significant increase in thrombolysis from HIFU treatment alone was seen as compared to the control. The clots treated with HIFU in combination with rt-PA, showed a 50% increase in the degree of thrombolysis compared to clots treated with rt-PA alone. In 2007, the same group conducted *in vivo* experiments, using the rabbit marginal ear vein, to see if the same effects could be achieved [32]. Slightly different HIFU parameters were used (1 MHz; 5% duty cycle; total acoustic power=40 W). Again, HIFU treatment alone showed no significant difference from the control group. In this setting, they could demonstrate a significant advantage of HIFU plus rt-PA (complete recanalization, the restoration of the blood flow) as compared to treatment with rt-PA alone (partial recanalization).

Holland et al. [20] explored various ultrasound settings (120 kHz or 1 MHz, continuous wave vs pulsed wave, duty cycle, time duration) *in vitro* to determine the thrombolytic efficacy of ultrasound treatment with and without rt-PA. Their results are similar to Frenkel et al. [18] and Stone et al. [32]. They demonstrated that treatment with ultrasound and rt-PA significantly increases thrombolysis by as much as 104% as compared to treatment with rt-PA alone. Also, no significant thrombolysis was observed for treatment with ultrasound alone as compared to the control. They found no clear dependence of thrombolysis on duty cycle but clot mass loss increased with the square root of the treatment duration.

Xie et al. [31] studied the effectiveness of low and high intensity ultrasound (1.0 MHz, low: 0.4 to 0.6 W/cm² continuous wave, high: 10.0 W/cm² pulsed-wave mode at 10% duty

cycle) in combination with microbubbles in the recanalization of thrombi in canines. Notably, this study does not include thrombolytic drugs. They were able to demonstrate that ultrasound with microbubbles, at all intensity levels, had a higher recanalization rate than ultrasound alone, with the higher intensities being the most effective.

Pulsed high intensity focused ultrasound (HIFU) has also been shown to accelerate thrombolysis without the addition of thrombolytic drugs or microbubbles [19, 17]. Rosenschein et al. [19] used a therapeutic transducer with an integrated ultrasound imaging transducer to study *in vitro* clots, which were inserted in bovine arterial segments. Optimal ultrasound wave parameters were chosen to be duty cycle=1:25, pulse length=200 *ms*, and $I_{SPTA} = 40 \text{ W/cm}^2$ at 500 *kHz*. At this ultrasound setting, thrombolysis efficiency (defined as the ratio between the weight of the lysed clot and the initial clot) was 91%. The ultrasound imaging during showed cavitation clouds during insonation, suggesting that HIFU-induced cavitation mechanisms might play an important role in sonothrombolysis. This is the subject of the next section.

1.2.3 Acoustic cavitation mechanisms

Acoustic cavitation is a general term used to describe the dynamical response or formation of a bubble or group of bubbles driven by an acoustic field. It is typically divided into two categories describing the bubble behavior: stable cavitation and inertial (or transient) cavitation. In stable cavitation, the bubble undergoes smooth, sustainable oscillations about an equilibrium radius. Increasing the peak negative pressure of the sound field leads a bubble to grow rapidly followed by violent collapses, see Fig. 1.2. This is termed inertial cavitation.

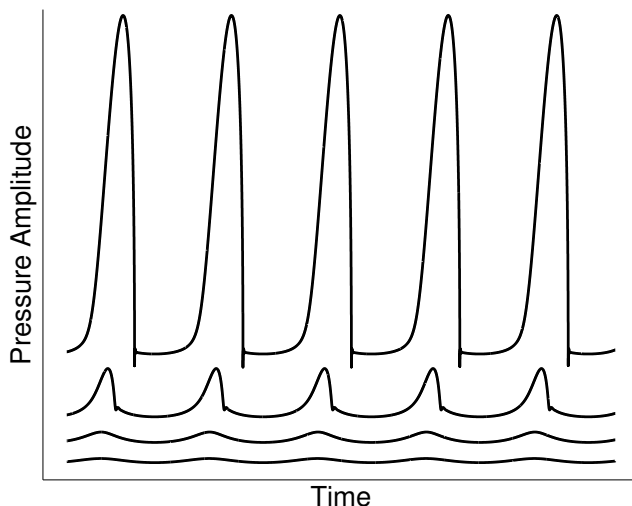


Figure 1.2: The radial responses of a bubble (R_0 fixed) over time for various amplitudes of the applied pressure wave (sinusoidal). The bubble goes from stable to inertial cavitation as the pressure amplitude is increased.

Several recent studies have investigated the role acoustic cavitation plays during thrombolysis and found it to be a significant contributor to clot destruction [33, 34, 35]. All of these studies use thrombolytic agents in combination with microbubbles to enhance the clot break up. The authors propose several known cavitation mechanisms as potential explanations for the enhancement of thrombolysis during ultrasound exposure. Mechanisms associated with stable cavitation include microstreaming and localized stresses. Inertial cavitation mechanisms includes microjetting and localized heating.

Datta et al. [34] investigated stable and inertial cavitation effects on blood clots during ultrasound exposure *in vitro*. They found that stable cavitation alone, as opposed to both stable and inertial cavitation, was more effective at clot lysis, in the presence of rt-PA. Possible stable cavitation mechanisms suggested were mechanical damage inside the blood clot (which exposes more binding sites for thrombolytic drugs) and micropumping of clot material away from the clot (increasing clot mass loss).

Prokop et al. [35] also suggests that stable cavitation may play a more important role than inertial cavitation. They investigated cavitation-based mechanisms during ultrasound exposure with and without rt-PA and in the presence and absence of ultrasound contrast agents (microbubbles). Ultrasound plus microbubbles (with no rt-PA) resulted in no significant clot mass loss (the measure of clot destruction used in this study.) The authors suggest that this is due to the observed limited duration of inertial cavitation.

Sonothrombolysis with the addition of microbubbles and no fibrinolytic drugs has also been achieved *in vitro* [15, 16, 21] and *in vivo* [24, 29, 31] (see also [36] and the citations

within). Eliminating the use of rt-PA in this treatment method will likely increase the treatment window and the number of patients eligible for this treatment protocol. While these studies show microbubbles combined with ultrasound can enhance clot destruction, they only make reference to studies where rt-PA is used as to the potential cavitation mechanisms. Significant work is needed in this area to identify the roles that stable and inertial cavitation play during microbubble enhanced thrombolysis (in the absence of thrombolytic agents.)

1.2.4 Hemorrhagic stroke

Recently, there has been increasing attention for the use of ultrasound for hemorrhagic stroke by means of hematoma lysis. A pilot study of nine patients, conducted by Newell et al. [37], showed encouraging results for the lysis and drainage of a blood clot (hematoma) using an ultrasound catheter design for the treatment of ischemic stroke plus *rt-PA*. In the future, a larger study and development of a specific system for this type of stroke are needed.

1.2.5 Assessing mechanical damage

The goal of this dissertation is to assess the plausibility of mechanical damage as an important mechanism for thrombolysis acceleration in high intensity focused ultrasound (HIFU) with microbubbles present. Two methods are developed to estimate the damage. To achieve this goal, the dynamics of single bubble wholly embedded in a blood clot, and one external to the blood clot are analyzed. The description of the bubble dynamical model used is described in the next section.

1.3 Bubble dynamics

The bubble dynamics used in this work to describe a microbubble in or near a blood clot are presented in depth in this section. A standard method in analyzing the bubble dynamics, which easily connects with physical experiments, is to examine the frequency content of the radiation pressure.

1.3.1 Keller-Miksis Equation

The bubble dynamics presented in this work are modeled by the Keller-Miksis equation with the linear Kelvin-Voigt model for a viscoelastic material, developed by Yang and Church [38]. Yang and Church derive the Keller-Miksis equation by employing asymptotic solutions of the volumetric flow rate and the pressure in the near field and the far field. The derivation begins with the continuity equation and the conservation of radial momentum in spherical coordinates. In the near field ($r = O(R)$), where r is the radial axis and R is the position of

the gas-tissue or gas-liquid interface), the surrounding material is considered incompressible. The pressure distribution is found from the Bernoulli integral. In the far field ($r \gg R$), the governing equation is the linear acoustic equation, as the pressure and density fluctuations are small and the components of the stress are negligible. These solutions are matched in an intermediate zone, resulting in the bubble dynamical equations.

The Keller-Miksis equation was chosen because it can account for large amplitude bubble oscillations, like those commonly observed during high intensity focused ultrasound. The Kelvin-Voigt model for the viscoelastic material is chosen based on the available data in the megahertz frequency regime used in that work. The one-dimensional Kelvin-Voigt model is represented conceptually by a purely elastic spring and purely viscous damper connected in parallel, see Fig. 1.3. The constitutive relation is $\sigma(t) = \mu d\epsilon(t)/dt + G\epsilon(t)$, where $\sigma(t)$ is the stress and $\epsilon(t)$ is the strain. The shear modulus and viscosity of the viscoelastic material are G and μ , respectively. In this work, the viscoelastic material is used to model a blood clot.

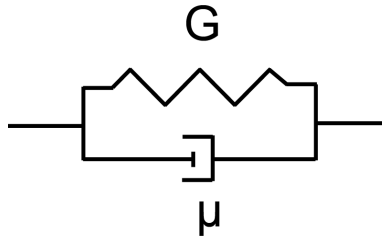


Figure 1.3: The conceptual representation of a Kelvin-Voigt material where G and μ are the shear modulus and viscosity of the viscoelastic material, respectively.

The nonlinear oscillations of a bubble in a soft tissue are found by numerically integrating the following equations:

$$\left(1 - \frac{\dot{R}}{c}\right) R \ddot{R} + \frac{3}{2} \left(1 - \frac{\dot{R}}{3c}\right) \dot{R}^2 = \left(1 + \frac{\dot{R}}{c}\right) \frac{P_a - P_I}{\rho} + \frac{R}{\rho c} \frac{d}{dt} [P_a - P_I], \quad (1.1)$$

where

$$P_a - P_I = p_{g0} \left(\frac{R_0}{R}\right)^{3\kappa} - \frac{2\sigma}{R} - P_0 + P(t) - \frac{4G}{3R^3} (R^3 - R_0^3) - \frac{4\mu\dot{R}}{R}, \quad (1.2)$$

$$\frac{d}{dt} [P_a - P_I] = \left(\frac{2\sigma}{R} - 3\kappa p_{g0} \left(\frac{R_0}{R}\right)^{3\kappa}\right) \frac{\dot{R}}{R} + \frac{dP(t)}{dt} - 4G \frac{R_0^3 \dot{R}}{R^4} - 4\mu \left(-\frac{\dot{R}^2}{R^2} + \frac{\ddot{R}}{R}\right). \quad (1.3)$$

Here R is the bubble radius, R_0 is the bubble equilibrium radius, the dot denotes a time derivative, c is the speed of sound in the surrounding material, σ is the surface tension, ρ is the density, P_a is the pressure at the bubble surface, and P_I is the pressure at infinity.

The gas inside the bubble is assumed to be ideal, i.e. the pressure inside the gas bubble is given by $P_g = p_{g0} (R_0/R)^{3\kappa}$, where κ is the polytropic index and $p_{g0} = 2\sigma/R_0 + P_0$ is the gas pressure in the bubble at equilibrium.

Yang and Church use their model to study the effects of elasticity on the bubble dynamics. They show that the presence of elasticity in the bubble dynamics equations reduces the nonlinearity of the radial dynamics and increases the inertial cavitation threshold. The sound emissions of the bubble were also studied. The method by which it is done is used in this work as well and is explained in the next section.

1.3.2 Sound emission

For an optically unobservable bubble, as in the case of a bubble in a nontransparent tissue, detection of the bubble's acoustic emission is often the best way to gain information about it. Experimentally, a passive or active cavitation detector system can be employed for this purpose. A typical passive cavitation detection (PCD) setup includes a PCD transducer, a computer for acquisition and storage, preamps and filters. The frequency content of the acquired data is obtained by taking the Fast Fourier Transform (FFT) at each time step. (The FFT is an efficient algorithm used to calculate the discrete Fourier Transform. Fourier transforms are commonly used to examine the frequency content of a signal.)

The presence of harmonics and ultraharmonics of the driving frequency is indicative of stable cavitation. As the inertial cavitation threshold is approached (for example, by increasing the pressure amplitude), there is an increase in the subharmonic emissions. Inertial cavitation is noted by an increase in the broadband noise.

Mathematically, the acoustic pressure radiated by the bubble is given by

$$P_s(t) = \rho \frac{R}{r} \left(\ddot{R}R + 2\dot{R}^2 \right) \quad (1.4)$$

where R is the bubble radius at time t and r is the distance from the center of the bubble [39]. The FFT of P_s is used to determine the frequency content of the signal, which can then be compared to the experimentally obtained data.

Eqn. 1.4 is derived from Euler's equation, which is used to relate the pressure in the liquid to the fluid velocity for the spherically symmetric case. For an incompressible fluid, the pressure at a distance r from the bubble center is comprised of two terms: the acoustic pressure and the kinetic wave. Far from the bubble the kinetic term is negligible, giving the acoustic pressure radiated by the bubble as Eqn. 1.4.

1.4 Summary of original contributions

This dissertation is a first step in understanding how mechanical damage from cavitation can be employed to enhance ultrasound mediated medical treatments. Mechanical damage

is not only seen in sonothrombolysis but in many other biomedical ultrasound applications, such as kidney stone ablation using shock wave lithotripsy. The goal of this dissertation is to examine the viability of mechanical damage as a plausible cavitation mechanism to enhance ultrasound mediated thrombolysis with the addition of microbubbles.

Experimental data shows damage to the fibrin clot structure and red blood cell lysis providing the motivation for the theoretical calculations presented here. Two independent methods are derived to estimate the mechanical damage caused by a cavitating bubble. The first method examines the stretch of individual fibrin fibers of the blood clot and estimates the number of broken fibers as a bubble embedded in the blood clot grows to its maximum radius. This method assumes no damage is occurring to the clot structure (i.e. there is no change in the radial dynamics equations) as the bubble expands however it is predicting that fibers will break, which will alter the equations for the bubble dynamics. To account for fibers breaking and the lysing of cells, the bubble dynamics equations could be altered by adding another term. Altering the bubble dynamics equation is equivalent to changing the work-energy statement. This motivates the second method, which is an energy based approach. Both methods use the notion of quantifying damage in terms of energy needed to cause the damage and provide consistent results. The energy method is extended to the scenario of a bubble outside of the blood clot that collapses asymmetrically creating a jet towards the clot.

To further understand the possible cavitation mechanisms present in a complete experimental setup, the effects of the physical properties of skull bone when a HIFU wave propagates through it are examined. The dynamics of a test bubble placed at the focus are used as a means to understand the pressure field. The type of cavitation present is explored by means of the sound emitted by the bubble. The amount of damage in the area surrounding the focus is examined for various initial bubble sizes. The pressure at the focus depends strongly on the density of the skull, with the pressure amplitude at the focus of the wave increasing as the density of the calvaria the wave passes through decreases. The maximum amount of energy available to cause damage to a blood clot increases as the density of the calvaria decreases, in general. Also, as initial bubble radius increases, there is a shift from stable to inertial cavitation, and this is evident in the acoustic power spectrum as well as the bubble dynamics. We find that there is usually a mixture of both stable and inertial cavitation present.

Chapter 2

Mechanical Damage to a Blood Clot from Bubble Dynamics

2.1 Introduction

Stroke is one of the leading causes of death in the United States, with 87% of all strokes being ischemic [40]. Currently, there are several FDA approved treatments for ischemic stroke, including thrombolytic agents, mechanical removal, angioplasty and stenting. Recombinant tissue plasminogen activator (rt-PA) is the only FDA approved thrombolytic drug treatment for ischemic stroke [41]. There are however severe limitations in the administration of the drug, most notably the requirement that the drug be delivered within 3 hours of the onset of the stroke. Recently, it was recommended that the time requirement be extended from 3 hours to 4.5 hours [9], but it has not been FDA approved yet. It is estimated that only 1-5% of all ischemic stroke patients taken to emergency rooms are administered rt-PA [10, 11].

Ultrasound has been shown *in vitro* [14, 13, 12, 20, 18, 19, 17] and *in vivo* [22, 23, 25, 27, 28, 26, 30, 32] to accelerate thrombolysis. Most of these studies show the enhancement of thrombolysis by ultrasound in conjunction with rt-PA or other thrombolytic agents. Pulsed high intensity focused ultrasound (HIFU) has also been shown to accelerate thrombolysis without the addition of thrombolytic drugs [19, 17, 21, 31].

Acoustic cavitation has been identified as a significant contributor to clot lysis [33]. Several mechanisms relying on inertial or stable cavitation have been proposed as potential explanations for the enhancement of thrombolysis during ultrasound exposure. Datta et al. [34] investigated stable and inertial cavitation effects on blood clots during ultrasound exposure *in vitro*. They found that stable cavitation alone, as opposed to both stable and inertial cavitation, was more effective at clot lysis, in the presence of rt-PA. Possible stable cavitation mechanisms suggested were mechanical damage inside the blood clot (which exposes more binding sites for thrombolytic drugs) and micropumping of clot material away from the clot (increasing clot mass loss). Prokop et al. [35] also suggests that stable cavitation may play

a more important role than inertial cavitation. They investigated cavitation-based mechanisms during ultrasound exposure with rt-PA and in the presence and absence of ultrasound contrast agents.

The goal of this chapter is to investigate the potential for cavitation to cause mechanical damage to a blood clot. Two methods are presented to estimate the number of fibers broken in a blood clot mechanically disturbed by a bubble. One is based on the stretch of individual fibers and the other is based on the energy available to break individual fibers. Experimental work provides the motivation for these calculations.

The chapter is arranged as follows. We first describe experiments aimed at probing the presence of mechanical damage associated with cavitation. We then develop the two approaches we use to estimate the mechanical damage caused by a bubble embedded within a blood clot. The second method is then extended to the case of a bubble outside but near the clot. Finally we compare the two methods and discuss the future scope of this work.

2.2 Materials and Methods

The experiments described in this section were led by Dr. Thilo Hoelscher's group at the University of California, San Diego, with participation by the author..

2.2.1 Clot Model

Venous whole blood was drawn from a healthy, unmedicated donors and transferred into citrate tubes. An appropriate IRB approval was in place. 2.0 ml of citrate blood was transferred into a borosilicate glass tubes. 180 μl CaCl_2 (5.68 mM) was added. After the CaCl_2 had been added to the citrate blood and mixed for 10 seconds, 0.5 ml of the solution was transferred into a 1.0 ml glass syringe, in which a silk thread had been placed. After incubation for 3 hours the clot was organized around the thread (Figure 2.1). The thrombus was incubated for 3.0 hours in a preheated (37°C) water bath. The average clot weight was about 255 mg \pm 10% without the thread.

2.2.1.1 Testing Tube

In the following, the clots were transferred into a polyethylene (PE) test tube. Ultra thin-walled PE non-shrink tubing (Advanced Polymers Inc., USA) was used. The tubes have an inner diameter of 4.2 mm and a wall thickness of 25 μm . Due to its ultra thin walls, the tubing has preferred acoustic properties compared to other polyester compounds. The described tubing is commercially available and the specifications (inner diameter, wall thickness) can be customized as needed, however, such tubing does not provide the wall elasticity of an artery.

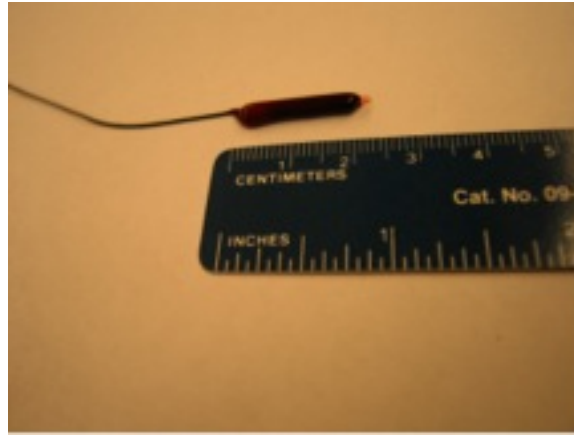


Figure 2.1: Thrombus on a silk thread. Figure courtesy of T. Hoelscher.

2.2.2 Experimental Setup

The PE test tube with the clot inside was placed into a unidirectional flow system with a pulsatile flow pump, integrated in a pre-heated water tank (Figure 2.2). From the main reservoir (500 ml glass beaker) the outlet tubing (approx. length: 75 cm) was connected with the PE tubing after passing the pulsatile flow pump. The pulsatile flow is generated using a simple peristaltic pump (Harvard Apparatus, USA). This set up allows for the exchange of only the PE tube without detaching other parts. Prior to insonation, the entire set up was immersed into the pre-heated water tank. Both the proximal and distal part of the PE tube was connected to a T-connector from which a second PE tube was used as a control for the experiment. The ultrasound transducer was immersed into the water and mounted above the PE test tube at a distance of 5.0 cm. The mounting device enables free rotation of the transducer in all three dimensions. Phosphate buffered saline (PBS) was used as a fluid for the flow system. The main reservoir was filled with PBS and placed on a mixing plate to ensure a homogenous mixture. The tank itself was filled with deionized, degassed water and was heated by a heating device inside the tank to maintain the temperature at 36°C.

2.2.3 Acoustic Field Characterization / Passive Cavitation Detection

As needed, acoustic measurements during sonothrombolysis are performed using a 0.2 mm needle hydrophone (Precision Acoustics, Dorchester, United Kingdom), including a buffer amplifier. The hydrophone was calibrated over the range of 1-20 MHz in 1 MHz increments. The acoustic signals were registered using an oscilloscope. The digitized signals were transferred to a PC. A customized MatLab™ based program was used for scan data analysis. Commonly, for each measurement point, four different acoustic parameters were assessed simultaneously: a) Maximum Intensity (W/cm^2), b) Minimum Negative Pressure (Pa), c)

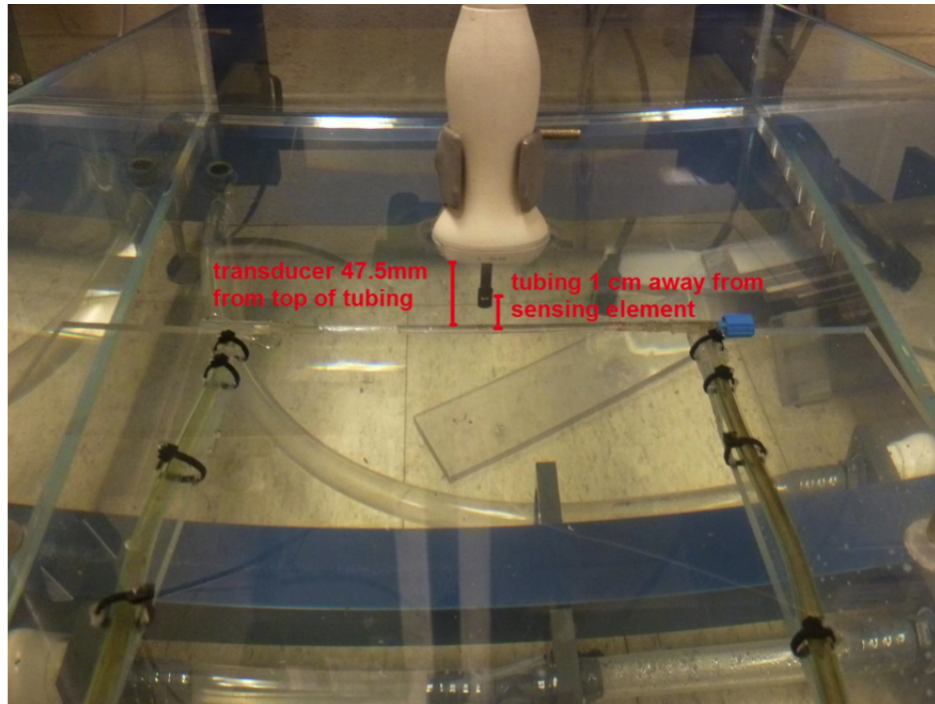


Figure 2.2: Top view inside the tank, showing inlet/outlet, test tube, transducer positioned above and PCD hydrophone positioned aside. Figure courtesy of T. Hoelscher.

Maximum Positive Pressure (Pa), and c) Maximum Peak-to-Peak Pressure (Pa). Based on these values, further parameters such as Mechanical Index, Spatial Time Average Intensity, Voltage or Area of Maximum Intensity etc. can be further calculated. For cavitation measurements we used a Sonic Concepts Y105 hydrophone. It has a large bandwidth between 10 KHz and 15 MHz to cover stable cavitation signals in the sub MHz range as well as inertial cavitation signals above the MHz threshold. The hydrophone has 2 side-facing, non-focused elements.

2.3 Experimental Images

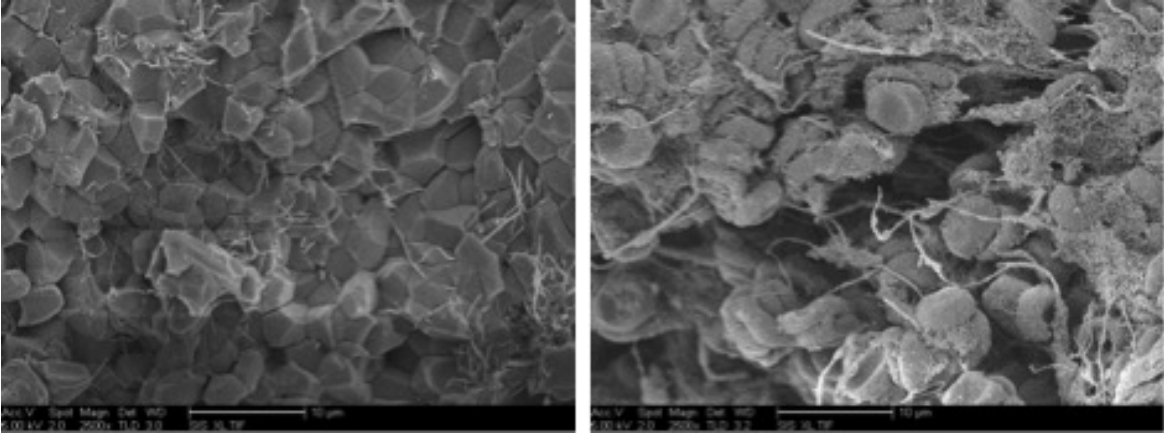
The experimental images presented in this section provide the motivation for the theoretical and numerical estimations of mechanical damage presented in the following section.

2.3.1 Scanning Electron Microscopy

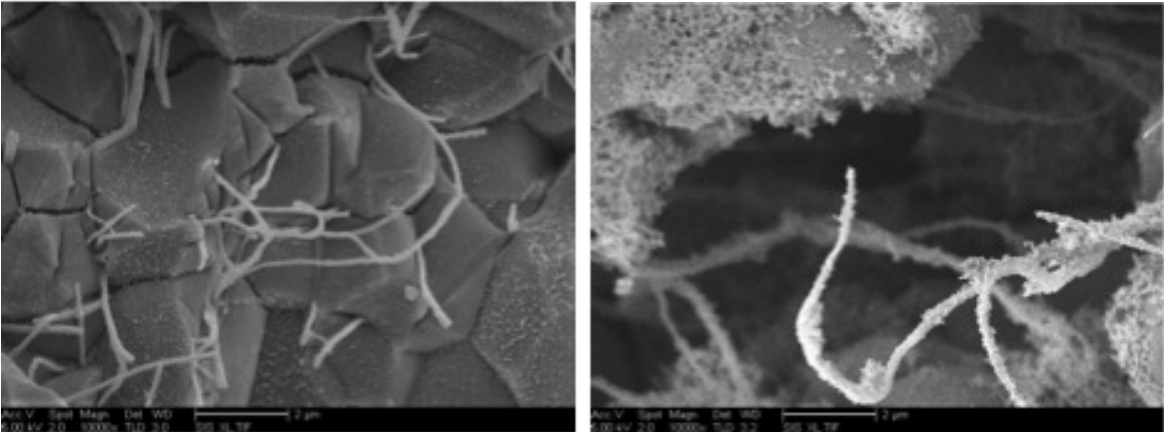
Scanning electron micrographs of human citrate blood clots are shown in Fig. 2.3. The images in the left column are different magnifications of a clot prior to HIFU insonation. The images in the right column are of a blood clot subjected to a HIFU wave with the

following properties: 50% duty cycle, 100 *ms* pulse width, 220 *kHz* total frequency, 235 *W* acoustic power, and 10 *s* insonation duration. In previous experiments, this ultrasound setting has been shown to cause significant clot lysis.

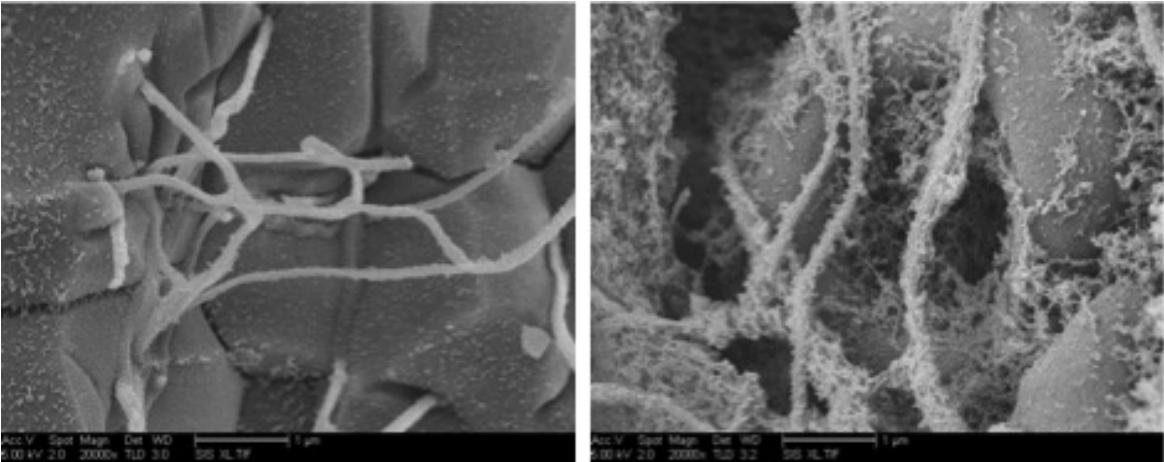
Post insonation, broken fibrin fibers are easily seen, see Fig. 2.3a right. Also, the ‘dusty’ pattern on the surface of the visualized fibrin fibers and red blood cells represents cellular matrix that has been released due to cell lysis. The damage observed is due to mechanical damage rather than chemical damage, as no drugs (for example rt-PA) have been added to the system. We note that no microbubbles were intentionally added during these experiments.



(a) 2500x magnification



(b) 10000x magnification



(c) 20000x magnification

Figure 2.3: Scanning Electron Micrograph of a human citrate blood clot before HIFU treatment (left column) and after HIFU treatment (right column). The image shows a dense fibrin fiber network with numerous cells incorporated into the matrix. (Figure courtesy of G. Ahadi, Hoelscher group, UCSD.)

2.3.2 Acoustic Field

The passive cavitation detection (PCD) system allows for acoustic measurements. For the ultrasound setting described in the previous section, the following measurements at the focal point were made using the needle hydrophone: the spatial peak temporal average intensity, $I_{STPA} = 136.8 \text{ W/cm}^2$, the peak negative pressure, $P_{NEG} = 2.8 \text{ MPa}$, and the peak positive pressure, $P_{POS} = 3.1 \text{ MPa}$. For cavitation measurements, the PCD system can detect the presence of sub and ultraharmonics (stable cavitation) and increases in the broad band noise (inertial cavitation). For an example of the PCD data see Fig. 2.4.

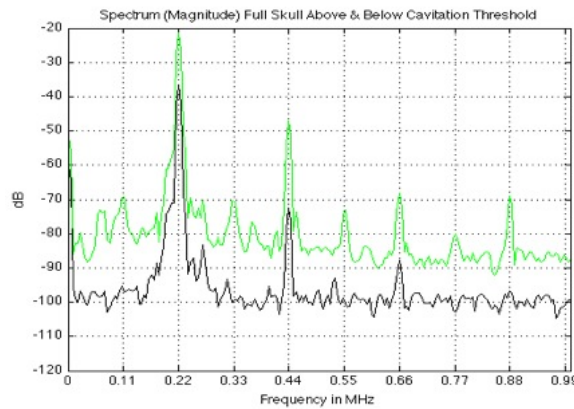


Figure 2.4: Spectrum plots for sonications below (800 kPa , black) and above (4.3 MPa , green) the cavitation threshold. Green plots exhibits sub & ultra harmonics (stable cavitation) and also broadband signal elevation (inertial cavitation). Lower plot was used as a baseline reference to calculate cavitation activities. (Figure courtesy of A. Voie, Hoelscher group, UCSD.)

2.3.3 Motivation for Mechanical Damage

As seen in Fig. 2.3a right, there is clearly damage to the fibrin network of the blood clot as well as lysis of red blood cells. No thrombolytic drugs were used in this study, therefore the damage is a result from mechanical effects. Mechanical damage to the blood clot could be a result from the ultrasound wave and/or cavitation. Several studies have shown that the presence of microbubbles and cavitation significantly increases clot lysis a compared to clots exposed to ultrasound alone [31]. This suggests that cavitation mechanisms play an important role in mechanical destruction of a blood clot.

2.4 Theoretical and Numerical Methods and Results

Now we approach the central question of how one may estimate the mechanical damage that a cavitation bubble might do to a clot. We do this both for the case of a bubble embedded in a clot, and for a bubble in the near vicinity of a clot, as the results are quite different owing to differences in the bubble dynamics as constrained (or not) by the much stiffer and more viscous clot material. In this section we describe two independent approaches to estimate mechanical cavitation damage to a blood clot. Both methods have in common a bubble dynamical model we describe after some discussion about what is known about clot architecture and clot physical properties. To estimate the damage, the clot is assumed to be a homogenous material and the region of damage estimated by the theoretical approaches is assumed to be spherically symmetric in the case where the bubble is embedded within the clot. This may not be the case and cracks may form if there is a weakness or other inhomogeneity in the clot structure.

2.4.1 Clot Properties

Fibrin mechanical properties have been studied extensively over the past four decades [42]. Blood clots are analogous to viscoelastic polymers, which possess strain and strain rate dependent physical properties. Much is known about bulk properties [43, 44] and single fibrin fiber properties [45, 46, 47, 48] for small strains and at small strain-rates or, equivalently, low frequencies. Roberts et al. [49] and Gerth et al. [50] examined the storage and loss moduli of coarse and fine fibrin clots (i.e. clots that contain no entrapped cells) at frequencies ranging from $\sim 1.0 \times 10^{-5} - 160 \text{ Hz}$ and found that these physical properties varied only slightly.

The mesoscale properties of a clot are a consequence of the clot architecture and the properties of fibrin fibers and embedded cells, if present. These mesoscale properties are conveniently framed in terms of shear modulus, G , and viscosity, μ , as appropriate for the viscoelastic model.

A very recent study by Huang et al. [51], examined the viscoelastic properties of a porcine thrombus using an instantaneous force approach. In this method, a solid sphere embedded in a blood clot undergoes insonation from a 1 MHz ultrasound transducer. The sphere is displaced by the instantaneous force from the transient acoustic wave [52] and the viscoelastic properties are determined from the spatiotemporal motion of the sphere. The shear modulus and viscosity obtained by this method for varying hematocrit levels ranges from $G = 173 \text{ Pa}$ and $\mu = 0.32 \text{ Pa} \cdot \text{s}$ for 40% hematocrit blood clots to $G = 620 \text{ Pa}$ and $\mu = 0.16 \text{ Pa} \cdot \text{s}$ for 0% hematocrit (plasma) blood clots. As the hematocrit is increased, there are more red blood cells that are entrapped in the fibrin fiber network. This will lead to a less dense fibrin matrix with larger pore size and a reduced number of cross-links, which makes the clot more deformable and have a smaller shear modulus [53]. These shear moduli values were compared to shear moduli obtained from a rheometer and were found to be in good agreement.

2.4.2 Bubble Dynamics

The Keller-Miksis equation with the linear Kelvin-Voigt model for viscoelastic material was developed by Yang and Church [38] to study single bubble dynamics in soft tissue. They used the model to investigate the effect of elasticity on the inertial cavitation threshold and subharmonic emissions of an oscillating bubble exposed to HIFU. The Keller-Miksis equation can account for large amplitude bubble oscillations [54], which may occur during HIFU insonation. The blood clot is modeled using a simple linear Kelvin-Voigt model for viscoelastic material (in one-dimension), which is represented conceptually by a purely elastic spring and purely viscous damper connected in parallel. The constitutive relation is $\sigma(t) = \mu d\epsilon(t)/dt + G\epsilon(t)$, where $\sigma(t)$ is the stress and $\epsilon(t)$ is the strain. The shear modulus and viscosity of the viscoelastic material are G and μ , respectively. The following equations describe the dynamics of a bubble in such a soft tissue model:

$$\left(1 - \frac{\dot{R}}{c}\right) R\ddot{R} + \frac{3}{2} \left(1 - \frac{\dot{R}}{3c}\right) \dot{R}^2 = \left(1 + \frac{\dot{R}}{c}\right) \frac{P_a - P_I}{\rho} + \frac{R}{\rho c} \frac{d}{dt} [P_a - P_I], \quad (2.1)$$

$$P_a - P_I = p_{g0} \left(\frac{R_0}{R}\right)^{3\kappa} - \frac{2\sigma}{R} - P_0 + P_A \sin \omega t - \frac{4G}{3R^3} (R^3 - R_0^3) - \frac{4\mu\dot{R}}{R}, \quad (2.2)$$

$$\frac{d}{dt} [P_a - P_I] = \left(\frac{2\sigma}{R} - 3\kappa p_{g0} \left(\frac{R_0}{R}\right)^{3\kappa}\right) \frac{\dot{R}}{R} + \omega P_A \cos \omega t - 4G \frac{R_0^3 \dot{R}}{R^4} - 4\mu \left(-\frac{\dot{R}^2}{R^2} + \frac{\ddot{R}}{R}\right). \quad (2.3)$$

In this equation, R is the bubble radius, R_0 is the bubble equilibrium radius, the dot denotes a time derivative, c is the speed of sound in the surrounding material, σ is the surface tension, ρ is the density, P_a is the pressure at the bubble surface, and P_I is the pressure at infinity. The gas inside the bubble is assumed to be ideal, i.e. the pressure inside the gas bubble is given by $P_g = p_{g0} (R_0/R)^{3\kappa}$, where κ is the polytropic index and $p_{g0} = 2\sigma/R_0 + P_0$ is the gas pressure in the bubble at equilibrium. The applied pressure from the HIFU field is here modeled by $P_A \sin \omega t$.

The following parameters are used throughout the paper: $P_0 = 1.01 \times 10^5 Pa$, $c = 1540 m/s$, $\rho = 1060 kg/m^3$, $\sigma = 0.052 N/m$, and $\kappa = 1.4$. These are the same parameters chosen by Yang and Church [38]. The viscoelastic properties of the clot are taken from Huang et al. [51]. Corresponding to the shear moduli they obtain (a range of $G = 173$ to $620 Pa$ depending on the hematocrit), the bubble dynamics differ by only hundredths of a micron. In the present work, unless noted, the shear modulus and viscosity of a clot are taken to be $G = 0.5 kPa$ and $\mu = 0.2 kg/(m \cdot s)$, respectively. The amount of damage done by a bubble to a clot is estimated as a function of the magnitude of the acoustic input, P_A , which is taken to be $P_A = 0.5, 1.0, \text{ and } 1.5 MPa$, see Fig 2.5.

In this study, we will consider a single bubble wholly surrounded by clot material using both methods to estimate mechanical damage to the clot. We will also consider a bubble outside the clot, but nearby, using the energy based approach.

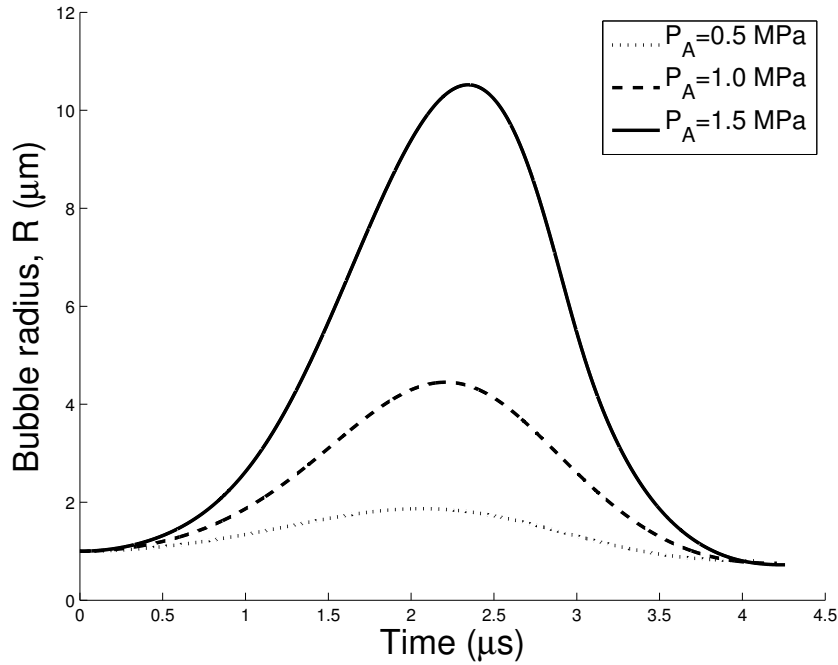


Figure 2.5: Dynamics of a single bubble wholly embedded in a blood clot, for various acoustic input amplitudes, $P_A = 0.5, 1.0, \text{ and } 1.5 \text{ MPa}$ for a bubble with initial radius $R_0 = 1 \mu\text{m}$.

2.4.3 Strain Method for Estimation of Cavitation Damage for an Embedded Bubble

Now we turn to the first of two independent methods we shall use to estimate cavitation damage, which is based on stretch of the principal molecules that give the clot its structure: fibrin. In this method, we examine the stretch of individual fibrin fibers as a bubble in an isotropic, viscoelastic material, with mean properties of the clot, expands to its maximum radius during HIFU. The bubble dynamics are calculated assuming no damage to the blood clot is occurring. The motion within the clot material is affine and the fibrin fibers surrounding the oscillating bubble will deform and the principal stretches can be calculated. In general for spherical coordinates, a deformation can be described by the following set of equations

$$\begin{aligned}
 r(t) &= r(r_0, \theta_0, \phi_0, t_0, t) \\
 \theta(t) &= \theta(r_0, \theta_0, \phi_0, t_0, t) \\
 \phi(t) &= \phi(r_0, \theta_0, \phi_0, t_0, t)
 \end{aligned} \tag{2.4}$$

where subscript 0 denotes the quantity evaluated at the initial time, t_0 (i.e. $r_0 = r(t_0)$).

The eigenvalues, λ_i , of \mathbf{V} are known as the principal stretches and eigenvalues of \mathbf{B} are λ_i^2 . In spherical coordinates the matrix, \mathcal{B} , associated with tensor \mathbf{B} is

$$\mathcal{B} = \begin{bmatrix} \mathcal{B}_{rr} & \mathcal{B}_{\theta r} & \mathcal{B}_{\phi r} \\ \mathcal{B}_{r\theta} & \mathcal{B}_{\theta\theta} & \mathcal{B}_{\phi\theta} \\ \mathcal{B}_{r\phi} & \mathcal{B}_{\theta\phi} & \mathcal{B}_{\phi\phi} \end{bmatrix}$$

where

$$\begin{aligned} \mathcal{B}_{rr} &= \left(\frac{\partial r}{\partial r_0} \right)^2 + \left(\frac{1}{r_0} \frac{\partial r}{\partial \theta_0} \right)^2 + \left(\frac{1}{r_0 \sin \theta_0} \frac{\partial r}{\partial \phi_0} \right)^2 \\ \mathcal{B}_{\theta\theta} &= r^2 \left[\left(\frac{\partial \theta}{\partial r_0} \right)^2 + \left(\frac{1}{r_0} \frac{\partial \theta}{\partial \theta_0} \right)^2 + \left(\frac{1}{r_0 \sin \theta_0} \frac{\partial \theta}{\partial \phi_0} \right)^2 \right] \\ \mathcal{B}_{\phi\phi} &= r^2 \sin^2 \theta \left[\left(\frac{\partial \phi}{\partial r_0} \right)^2 + \left(\frac{1}{r_0} \frac{\partial \phi}{\partial \theta_0} \right)^2 + \left(\frac{1}{r_0 \sin \theta_0} \frac{\partial \phi}{\partial \phi_0} \right)^2 \right] \\ \mathcal{B}_{\theta r} = \mathcal{B}_{r\theta} &= r \left[\frac{\partial r}{\partial r_0} \frac{\partial \theta}{\partial r_0} + \frac{1}{r_0^2} \frac{\partial r}{\partial \theta_0} \frac{\partial \theta}{\partial \theta_0} + \frac{1}{r_0^2 \sin^2 \theta_0} \frac{\partial r}{\partial \phi_0} \frac{\partial \theta}{\partial \phi_0} \right] \\ \mathcal{B}_{\phi r} = \mathcal{B}_{r\phi} &= r \sin \theta \left[\frac{\partial r}{\partial r_0} \frac{\partial \phi}{\partial r_0} + \frac{1}{r_0^2} \frac{\partial r}{\partial \theta_0} \frac{\partial \phi}{\partial \theta_0} + \frac{1}{r_0^2 \sin^2 \theta_0} \frac{\partial r}{\partial \phi_0} \frac{\partial \phi}{\partial \phi_0} \right] \\ \mathcal{B}_{\phi\theta} = \mathcal{B}_{\theta\phi} &= r^2 \sin \theta \left[\frac{\partial \theta}{\partial r_0} \frac{\partial \phi}{\partial r_0} + \frac{1}{r_0^2} \frac{\partial \theta}{\partial \theta_0} \frac{\partial \phi}{\partial \theta_0} + \frac{1}{r_0^2 \sin^2 \theta_0} \frac{\partial \theta}{\partial \phi_0} \frac{\partial \phi}{\partial \phi_0} \right]. \end{aligned}$$

For this application

$$\mathcal{B} = \begin{bmatrix} r_0^4 (r_0^3 + R(t)^3 - R_0^3)^{-4/3} & 0 & 0 \\ 0 & \frac{1}{r_0^2} (r_0^3 + R(t)^3 - R_0^3)^{2/3} & 0 \\ 0 & 0 & \frac{1}{r_0^2} (r_0^3 + R(t)^3 - R_0^3)^{2/3} \end{bmatrix}.$$

The eigenvalues of \mathcal{B} , for this application, are easily read from the diagonal entries. Therefore, the principal stretches are

$$\begin{aligned} \lambda_r &= r_0^2 (r_0^3 + R(t)^3 - R_0^3)^{-2/3} \\ \lambda_\theta = \lambda_\phi &= \frac{1}{r_0} (r_0^3 + R(t)^3 - R_0^3)^{1/3} \end{aligned} \quad (2.6)$$

and the associated (engineering) strains are

$$\begin{aligned} \epsilon_r &= r_0^2 (r_0^3 + R(t)^3 - R_0^3)^{-2/3} - 1 \\ \epsilon_\theta = \epsilon_\phi &= \frac{1}{r_0} (r_0^3 + R(t)^3 - R_0^3)^{1/3} - 1. \end{aligned} \quad (2.7)$$

An alternative geometric derivation of the engineering strains is performed as a check, please see Appendix A.

At point P_t , a fiber in a general orientation is described in local spherical coordinates (ρ, β, α) centered at point P_t with the following evolution equations

$$\rho(t) = \rho_0 \left(r_0^4 (r_0^3 + R^3(t) - R_0^3)^{-4/3} \cos^2 \alpha_0 + \frac{1}{r_0^2} (r_0^3 + R^3(t) - R_0^3)^{2/3} \sin^2 \alpha_0 \right)^{1/2} \quad (2.8)$$

$$\beta(t) = \beta_0 \quad (2.9)$$

$$\alpha(t) = \tan^{-1} \left(\left(1 + \frac{R^3(t) - R_0^3}{r_0^3} \right) \tan \alpha_0 \right) \quad (2.10)$$

where $(\rho_0, \beta_0, \alpha_0)$ is the position and orientation of the fiber in the reference configuration, see Fig. 2.6. The stretch of a fiber oriented initially at an angle α_0 from the radial direction is

$$\lambda_{\alpha_0} = \sqrt{\lambda_r^2 \cos^2 \alpha_0 + \lambda_\theta^2 \sin^2 \alpha_0}. \quad (2.11)$$

It is known that the orientation of each fiber is random for a clot formed under no flow conditions [55]. Fibers align in the direction of strain [56] and therefore any fiber with $\alpha_0 \neq 0$ will tend toward the circumferential direction outside an expanding bubble.

The strain at which a single, fully cross-linked fibrin fiber ruptures, e_{crit} , has been found experimentally to be $e_{crit} = 147\%$ [46]. This value for the critical strain was found using a technique that combines atomic force microscopy (AFM) and fluorescence microscopy. In previous studies from the same group, the AFM tip speed was on the order of $1 \mu\text{m}/\text{s}$ and varying the tip speed by an order of magnitude did not affect the measurement values [45]. We note that the time scale is relatively slow compared to this application, however there is no available data in our frequency regime.

We relate this to stretch, λ_{crit} , and use (2.11) to define a critical angle, α_{crit} , given by

$$\alpha_{crit} = \pm \cos^{-1} \left(\pm \sqrt{\frac{\lambda_{crit}^2 - \lambda_\theta^2}{\lambda_r^2 - \lambda_\theta^2}} \right) \quad (2.12)$$

at which fibers would break for the given deformation from R_0 to $R(t)$. Hence, for fibers at P_0 outside of a bubble of radius R_0 , deformation of the bubble to $R(t) > R_0$ leads to greater alignment in the circumferential direction. Fibers that are aligned close enough to the circumferential direction ($\alpha_0 > \alpha_{crit}$ initially) will break.

The number density of ruptured fibers, n , in the vicinity of any point P_t is given by

$$n(r_0, R_0, R(t)) = \int_{\substack{\text{fibers that} \\ \text{exceed} \\ \text{critical strain}}} \rho_{fiber} f(\beta, \alpha, t) d^2\mathbf{R} \quad (2.13)$$

where ρ_{fiber} is the density of fibers per unit volume, $f(\beta, \alpha, t)$ is the Eulerian representation of the distribution function of fiber orientations, and \mathbf{R} is the axial vector in rectangular coordinates of the fiber located at P , therefore

$$\mathbf{R} = \begin{pmatrix} \rho \sin \alpha \cos \beta \\ \rho \sin \alpha \sin \beta \\ \rho \cos \alpha \end{pmatrix}$$

The total number of broken fibers, N , during the deformation of the bubble from R_0 to $R(t)$ is

$$N = \int_{R_0}^{\infty} n(r_0, R_0, R(t)) 4\pi r_0^2 dr_0.$$

We are interested in the total number of fibers broken as the bubble goes from its initial radius R_0 to its maximum radius, R_{max} , because at the maximum bubble radius, the strains on the fibers near the bubble surface will be at their maximum.

An alternative, Lagrangian representation of distribution function, f^* is

$$f^*(\beta_0, \alpha_0, t) = f(\beta, \alpha, t)|_{\mathbf{R}=\hat{\mathbf{R}}(\mathbf{R}_0, t)}$$

where $\hat{\mathbf{R}}(\mathbf{R}_0, t)$ is the coordinate map from reference to deformation configuration given in Eqns. 2.8-2.10. Szeri and Leal [57], provide an approach to compute $f^*(\beta_0, \alpha_0, t)$ in terms of the coordinate map from reference to deformed configurations of the local structure

$$\frac{f^*(\beta_0, \alpha_0, t)}{f^*(\beta_0, \alpha_0, 0)} = \frac{1}{\det(\nabla_0 \hat{\mathbf{R}}(\mathbf{R}_0, t))} \quad (2.14)$$

where ∇_0 is the gradient operator with respect to the reference configuration coordinates. For fiber orientation description used here, the evolution of the Lagrangian distribution function is given by

$$\frac{f^*(\beta_0, \alpha_0, t)}{f^*(\beta_0, \alpha_0, 0)} = \left[\frac{\partial(\beta, \alpha)}{\partial(\beta_0, \alpha_0)} \frac{\sin \alpha}{\sin \alpha_0} \right]^{-1}$$

where the standard notation for the Jacobian of a transformation is used,

$$\frac{\partial(\beta, \alpha)}{\partial(\beta_0, \alpha_0)} = \det \begin{bmatrix} \frac{\partial \beta}{\partial \beta_0} & \frac{\partial \alpha}{\partial \beta_0} \\ \frac{\partial \beta}{\partial \alpha_0} & \frac{\partial \alpha}{\partial \alpha_0} \end{bmatrix}.$$

For the evolution equations, given by Eqns. 2.8-2.10, the Jacobian is

$$\frac{\partial(\beta, \alpha)}{\partial(\beta_0, \alpha_0)} = \frac{\partial \alpha}{\partial \alpha_0} = \frac{r_0^3 (r_0^3 + R^3(t) - R_0^3)}{r_0^6 \cos^2 \alpha_0 + (r_0^3 + R^3(t) - R_0^3)^2 \sin^2 \alpha_0}.$$

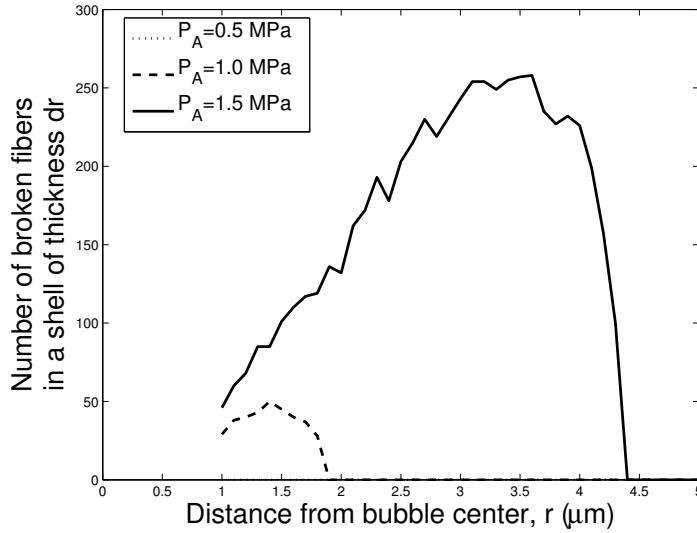
The Lagrangian form of the distribution function in terms of the coordinate map from reference to deformed configurations of the local structure is

$$\frac{f^*(\beta_0, \alpha_0, t)}{f^*(\beta_0, \alpha_0, 0)} = \frac{\sqrt{\lambda_1^2 \cos^2 \alpha_0 + \lambda_{23}^2 \sin^2 \alpha_0} r_0^6 \cos^2 \alpha_0 + (r_0^3 + R^3(t) - R_0^3)^2 \sin^2 \alpha_0}{\lambda_{23} r_0^3 (r_0^3 + R^3(t) - R_0^3)} = Fn(\alpha_0, r_0, t).$$

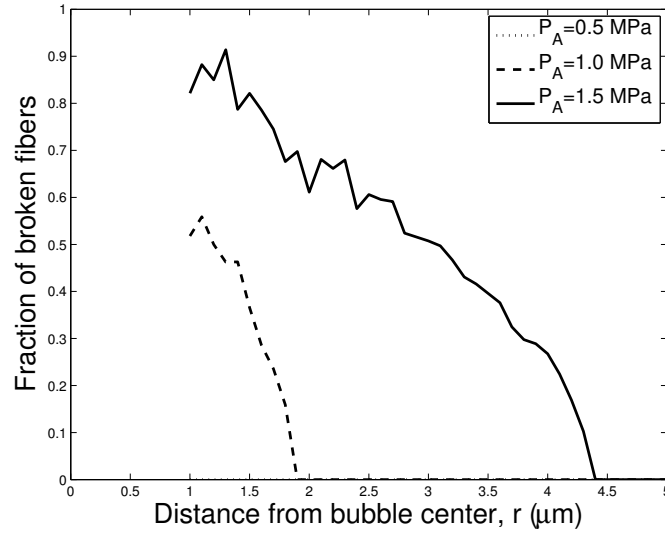
Initially the orientation distribution function is random, giving

$$f^*(\beta_0, \alpha_0, 0) = \frac{1}{4\pi}.$$

The resulting integral for the number density, found by substituting the new expression for $f^*(\beta_0, \alpha_0, t)$ into Eqn. 2.13, cannot be solved analytically. Instead to estimate the number density of fibers broken, a brute force calculation is used. First the number of fibers in a spherical shell of thickness dr is calculated and each fiber is assigned a random orientation in the reference configuration. For fibers with an initial orientation angle $\alpha_0 > \alpha_{crit}$, the fiber is broken in the given bubble deformation from R_0 to R_{max} , see Fig. 2.7.



(a)



(b)

Figure 2.7: The number and fraction of broken fibers for the bubble dynamics shown in Fig. 2.5. (a) Estimates of the number of broken fibers in a shell of thickness $dr = 0.1 \mu\text{m}$, plotted as a function of the distance from the bubble center in the reference configuration. (b) The fraction of broken fibers is also shown as a function of distance from bubble center. As expected, the highest fraction of fibers broken are close to the initial bubble surface.

The amount of energy required to break a single fibrin fiber is $W_{fiber} = 8 \times 10^{-13} J$ [46].

Again this value was obtained during a slow deformation of a single fibrin fiber, but the equivalent value during a rapid deformation is unknown at this time. The total amount of energy used breaking fibers is the number of fibers broken multiplied by the energy needed to break one fiber, see Table 2.1.

	P_A (MPa)		
	0.5	1	1.5
Number of fibers broken	0	350	6.0×10^3
Energy used (nJ)	0	0.28	4.80

Table 2.1: The total number of fibers broken and the energy used breaking them for various applied acoustic magnitudes.

We note that the exactly parallel calculations can be made using the strain rates, which are calculated by taking the time derivative of (2.7). This method is not shown because there is no available experimental data on strain rate dependency of the material properties of fibrin networks. However it may well be that breakage is determined by a strain-rate criterion rather than a stretch criterion at these conditions.

2.4.4 Work Method for Estimation of Cavitation Damage for an Embedded Bubble

The strain method uses the bubble dynamics assuming no damage is occurring to the clot structure, however it suggests that fibrin fibers will break during the expansion of the bubble from R_0 to a sufficiently large R_{max} . To account for the breaking of fibrin fibers (and lysing of red blood cells) perhaps some modification could be made to the Keller-Miksis equation. This motivates our next method, an independent energy based approach.

Let us first examine the bubble dynamics for the case of an incompressible fluid, we do this by letting $c \rightarrow \infty$ in 2.1-2.3 to obtain

$$R\ddot{R} + \frac{3}{2}\dot{R}^2 = \frac{1}{\rho} \left(p_{g0} \left(\frac{R_0}{R} \right)^{3\kappa} - \frac{2\sigma}{R} - P_0 + P_A \sin \omega t - \frac{4G}{3R^3} (R^3 - R_0^3) - \frac{4\mu\dot{R}}{R} \right).$$

This equation can be understood as a rate formulation of a work-energy statement, the rate of change of the liquid kinetic energy is equal to the difference in the rate of work being applied to the liquid outside the bubble by the pressure at infinity, P_∞ and the pressure at the bubble surface, P_L . The power is

$$4\pi R^2 \dot{R} P_L - \lim_{r \rightarrow \infty} 4\pi r^2 \frac{R^2}{r^2} \dot{R} P_\infty = 4\pi R^2 \dot{R} (P_L - P_\infty)$$

where

$$P_L = P_g - \frac{2\sigma}{R} - \frac{4G}{3R^3} (R^3 - R_0^3) - \frac{4\mu\dot{R}}{R}$$

and $P_\infty = P_0 - P_A \sin \omega t$.

The work done by individual terms can be understood by integrating with respect to time. The work done on the liquid outside the bubble by the acoustic wave as the bubble radius changes from R_0 at time $t_0 = 0$ to $R(t)$ at time t is

$$W_{AC} = -4\pi \int_0^t P_\infty R^2 \dot{R} dt. \quad (2.15)$$

The work done by the gas pressure, as the bubble changes from R_0 to $R(t)$ is

$$\begin{aligned} W_G &= 4\pi \int_0^t P_g R^2 \dot{R} dt \\ &= \frac{4p_{g0}\pi}{3(\kappa - 1)} \left(R_0^3 - \left(\frac{R_0}{R} \right)^{3\kappa} R^3 \right). \end{aligned}$$

The work done by the surface tension as R_0 to $R(t)$ is

$$\begin{aligned} W_\sigma &= 4\pi \int_0^t \frac{2\sigma}{R} R^2 \dot{R} dt \\ &= 4\pi\sigma (R^2 - R_0^2). \end{aligned}$$

The elastic energy stored in the surrounding fluid (which is viscoelastic when $G \neq 0$) as R_0 to $R(t)$ is

$$\begin{aligned} W_{SE} &= 4\pi \int_0^t \frac{4G}{3R^3} (R^3 - R_0^3) R^2 \dot{R} dt \\ &= \frac{16\pi}{9} G R_0^3 \left(\frac{R^3}{R_0^3} - 1 + 3 \ln \frac{R}{R_0} \right) \end{aligned}$$

and the energy lost to viscous effects in the surrounding fluid as R_0 to $R(t)$ is

$$\begin{aligned} W_{VL} &= 4\pi \int_0^t \frac{4\mu\dot{R}}{R} R^2 \dot{R} dt \\ &= 16\pi\mu \int_0^t R \dot{R}^2 dt. \end{aligned}$$

Note that the stored energy and the viscous loss can also be calculated by the integral of the stress power; in tensor notation this is

$$W_{SE} + W_{VL} = \int_{t=0}^t \int_V \nabla \cdot (\boldsymbol{\tau} \mathbf{v}) dV dt, \quad (2.16)$$

where $\boldsymbol{\tau}$ is the stress tensor, \mathbf{v} is the velocity field, ∇ is the divergence and V is the volume of the clot material outside the bubble [58]. Because the material is incompressible, $\tau_{rr} = 2(G\gamma_{rr} + \mu\dot{\gamma}_{rr})$ where $\dot{\gamma}_{rr} = -2R^2\dot{R}/r^3$ and $\gamma_{rr} = -2(R^3 - R_0^3)/(3r^3)$ [38].

At the maximum bubble radius, R_{max} , the kinetic energy of the liquid is zero and therefore the work done must sum to zero, giving the equation

$$0 = W_{AC} + W_G - W_\sigma - W_{SE} - W_{VL} \quad (2.17)$$

where each of these terms is evaluated at the time at which the radius is maximum, t_{max} .

For the compressible case, at the maximum bubble radius, the kinetic energy in the liquid is not zero (there are acoustic waves going off to infinity) so the energy balance given in (2.17) is only approximate,

$$0 \approx W_{AC} + W_G - W_\sigma - W_{SE} - W_{VL}. \quad (2.18)$$

This energy balance can be evaluated for a bubble embedded in a blood clot ($G = 0.5 \text{ kPa}$, $\mu = 0.2 \text{ Pa}\cdot\text{s}$), where the bubble dynamics do not account for damage during bubble growth (as in the previous method). This is a lower bound on the bubble radius. The energy balance can also be evaluated for a bubble in blood ($G = 0 \text{ Pa}$, $\mu = 0.005 \text{ Pa}\cdot\text{s}$). In a sense, this represents a clot that has been completely destroyed and no further damage can be done, so this provides an upper bound on the bubble radius. Realistically, as a bubble embedded in a blood clot grows, fibrin fibers will break (and red blood cells will be lysed). This weakens the network decreasing the shear modulus and lowers the hematocrit, thus decreasing the viscosity, thus allowing for a larger bubble radius, see Fig. 2.8 .

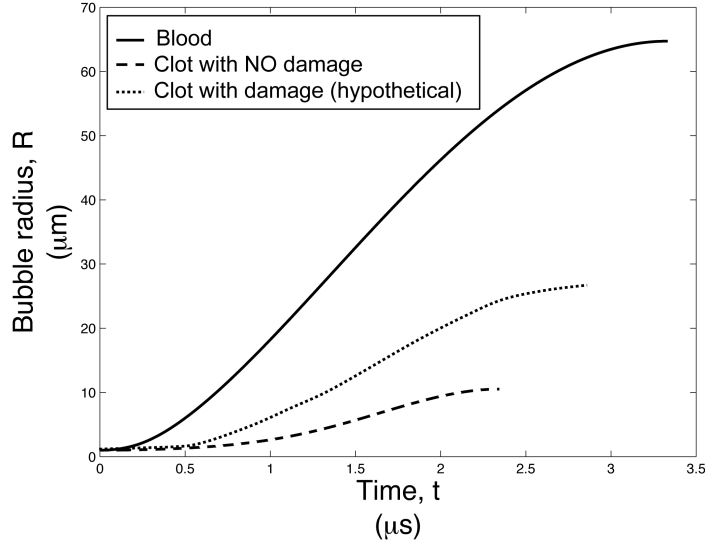


Figure 2.8: The bubble dynamics for a bubble in blood and the dynamics for a bubble wholly embedded in a blood clot, assuming no damage occurs during growth are plotted for $R_0 = 1\mu m$ and $P_A = 1.5 MPa$. These provide an upper and lower bound, respectively, for the expected bubble dynamics, accounting for damage to the blood clot, for a bubble wholly embedded in a clot.

For a bubble embedded in a blood clot, with dynamics given by Eqns. 2.1-2.3 (i.e. not accounting for damage to the clot) and for a bubble in blood, the energy terms in Eqn. 2.18 can be evaluated, see Table 2.2. For a bubble in an undamaged clot the work done by the gas pressure, the work done by the surface tension and the stored energy in the surrounding fluid are approximately zero, so at R_{max} the energy balance reduces to

$$W_{AC,ND} \approx W_{VL,ND} \quad (2.19)$$

where $W_{AC,ND}$ is the work done on the bubble from the acoustic wave and $W_{VL,ND}$ is the viscous loss. Similarly, for a bubble in blood, the work done by the gas pressure is approximately zero and the stored energy is exactly zero ($G = 0 MPa$), so the energy balance reduces to

$$W_{AC,Blood} \approx W_{\sigma,Blood} + W_{VL,Blood} \quad (2.20)$$

where $W_{AC,Blood}$ is the work done on the bubble (in blood) from the acoustic wave, $W_{\sigma,Blood}$ is the work done by the surface tension, and $W_{VL,Blood}$ is the viscous loss. For a bubble wholly embedded in a clot, which undergoes damage as the bubble grows, we can hypothesize a similar energy balance at R_{max} ,

$$0 \approx W_{AC,D} + W_{G,D} - W_{\sigma,D} - W_{SE,D} - W_{VL,D} - W_{D,D}$$

	Clot with No Damage	Blood
	$G = 0.5 \text{ kPa}, \mu = 0.2 \text{ Pa} \cdot \text{s}$	$G = 0 \text{ Pa}, \mu = 0.005 \text{ Pa} \cdot \text{s}$
$W_{AC} \text{ (nJ)}$	3.51	15.2
$W_G \text{ (nJ)}$	2.10×10^{-3}	2.22×10^{-3}
$W_\sigma \text{ (nJ)}$	7.72×10^{-2}	2.95
$W_{SE} \text{ (nJ)}$	3.27×10^{-3}	0
$W_{VL} \text{ (nJ)}$	3.46	11.8
$W_{AC} + W_G - W_\sigma - W_{SE} - W_{VL}$	-2.56×10^{-2}	0.472

Table 2.2: The work done on the bubble by the acoustic wave, the potential energy of the gas, the work done by surface tension, the stored energy in the fluid and the viscous loss to the fluid for a $R_0 = 1\mu\text{m}$ bubble for $P_A = 1.5 \text{ MPa}$.

where $W_{AC,D}$, $W_{G,D}$, $W_{\sigma,D}$, $W_{SE,D}$, and $W_{VL,D}$ are similarly defined as before but for a bubble in a blood clot that undergoes damage. The notable difference is the addition of a term, $W_{D,D}$, the energy lost to damage in the clot matrix from fibrin fiber breakage (and red blood cell lysis.) We imagine that $W_{G,D}$ and $W_{SE,D}$ will be approximately zero, as in the bounding cases, giving

$$W_{AC,D} \approx W_{\sigma,D} + W_{VL,D} + W_{D,D}. \quad (2.21)$$

A reasonable assumption is that the work done on a bubble in an undeformed clot from the acoustic wave, $W_{AC,ND}$, will be a lower bound for the work done on a bubble in a clot in which damage occurs from the acoustic wave, $W_{AC,D}$. The upper bound is the work done on a bubble in blood from the acoustic wave, $W_{AC,Blood}$, giving

$$W_{AC,ND} < W_{AC,D} < W_{AC,Blood}. \quad (2.22)$$

We recognize that this assumption breaks down for certain parameters (for example large bubbles and large applied pressure amplitudes) but is valid for the properties used in this work. Further work is ongoing as to when Eqn. 2.22 can be used. Therefore using Eqns. 2.19-2.21 and noting that the viscosity decreases with lower hematocrit gives

$$W_{VL,ND} < W_{VL,D} < W_{VL,Blood},$$

the inequality given in Eqn. 2.22 simplifies to

$$0 < W_{D,D} < W_{VL,Blood} - W_{VL,ND} + W_{\sigma,Blood} \quad (2.23)$$

using the reasonable expectation $W_{VL,D} - W_{VL,ND} + W_{\sigma,D} > 0$. This inequality, Eqn. 2.22, provides an upper bound on the energy lost to damage and hence on the amount of damage that can occur. The maximum amount of damage due to fibrin breakage can be calculated by dividing the left hand side of Eqn. 2.23 by the energy to break a single fiber

$W_{fiber} = 8 \times 10^{-13} J$. Of course, this neglects the potential damage associated with cell lysis if the hematocrit is not zero - more on this later. The results for various applied acoustic amplitudes is shown in Table. 2.3. For each applied acoustic amplitude, the upper bound on the number of fibers that can be broken, as determined by this method, is greater than the calculated number of fibers broken using the strain method. Therefore the strain method is consistent with the energy method.

	P_A (MPa)		
	0.5	1	1.5
$W_{AC,ND}$ (nJ)	7.19×10^{-3}	0.220	3.51
$W_{G,ND}$ (nJ)	1.18×10^{-3}	1.86×10^{-3}	2.10×10^{-3}
$W_{\sigma,ND}$ (nJ)	1.76×10^{-3}	1.32×10^{-2}	7.72×10^{-2}
$W_{SE,ND}$ (nJ)	2.07×10^{-5}	2.56×10^{-4}	3.27×10^{-3}
$W_{VL,ND}$ (nJ)	6.60×10^{-3}	0.209	3.46
$W_{AC,Blood}$ (nJ)	1.75	7.38	15.2
$W_{G,Blood}$ (nJ)	2.19×10^{-3}	2.21×10^{-3}	2.22×10^{-3}
$W_{\sigma,Blood}$ (nJ)	0.574	1.73	2.95
$W_{SE,Blood}$ (nJ)	0	0	0
$W_{VL,Blood}$ (nJ)	1.17	5.52	11.8
$W_{VL,Blood} - W_{VL,ND} + W_{\sigma,Blood}$ (nJ) (i.e. bound on energy available to break fibers)	1.74	7.04	11.3
Maximum bound on number of fibers broken (energy method)	2.18×10^3	8.80×10^3	1.41×10^4
Estimated number of fibers broken (strain method)	0	350	6.0×10^3

Table 2.3: The work done by the acoustic wave, the work done by the gas pressure, the work done by surface tension, the stored energy in the fluid and the viscous loss in the fluid for a bubble embedded in a clot with no damage and a bubble in blood for a $R_0 = 1\mu m$ bubble for various applied acoustic pressure magnitudes. The maximum number of broken fibers is computed using the upper bound from Eqn. 2.23 divided by the energy to break a single fibrin fiber.

2.4.5 Work Method for Estimation of Cavitation Damage for an External Bubble

The work-energy based approach can be adapted to the case of an external bubble near the clot surface. The bubble will grow to approximately the same size as a bubble far from a surface for various standoff distances [59, 60]. A bubble close enough to the clot will collapse asymmetrically and a jet will form directed at the clot. We assume that the kinetic energy

from the jet will go into the fiber network and be available to break fibers. For blood, the shear modulus and viscosity are $G = 0 \text{ Pa}$ and $\mu = 0.005 \text{ Pa} \cdot \text{s}$. Unlike the case of the bubble embedded in the clot material, we do not know the deformation induced in the clot material. Therefore, the viscous loss and stored energy in the matrix cannot be estimated.

For a free collapse, the maximum bound on the kinetic energy in the jet is the work done by the acoustic wave on the bubble as it expands from R_0 to R_{max} [61]. Here we have a forced collapse during which more work is done by the acoustic wave during the collapse after R_{max} . Calvisi et al. [62] compare the kinetic energy of the surrounding fluid for spherical and nonspherical collapses. They found an equivalent temperature for the kinetic energy at collapse for nonspherical bubbles and showed that the peak temperature for a spherical collapse is greater than for a nonspherical collapse by approximately this temperature-equivalent kinetic energy. This means that spherical collapses focus the acoustic energy into compression of the bubble contents more efficiently as no energy is ‘wasted’ on the jet. Therefore, for this work we use the conservative estimation of the work done by the acoustic wave during a spherical collapse as an upper bound to the amount of energy available to be transferred to the kinetic energy of the jet. Assuming the kinetic energy of the jet is then available to break fibers, an upper bound on the number of fibers broken can be estimated, see Table 2.4.

	$P_A \text{ (MPa)}$		
	0.5	1	1.5
$W_{AC} \text{ (nJ)}$	53.6	276	423
Bound on number of fibers broken	6.70×10^4	3.45×10^5	5.28×10^5

Table 2.4: The amount of work done by the acoustic wave on the bubble until collapse, W_{AC} , is transferred to the kinetic energy of the jet. This provides an upper bound for the number of fibers broken.

Note that the bubble external to the clot (Fig. 2.9) expands to a much larger radius owing to the smaller shear viscosity in blood plasma and the fact $G = 0 \text{ MPa}$ compared to the dynamics of a bubble in a clot (Fig. 2.5). The expansion is approximately spherical and the non-spherical collapse develops a peak fluid kinetic energy which scales with the work done by the expanding bubble plus additional work on collapse. Hence, collapse energies are far larger, and the energy available to break bonds leads to more fibrin breakages.

To calculate the acoustic work (Eqn. 2.15), the time of collapse must be determined. This is chosen to be the time when \dot{R} goes through zero from negative to positive as the bubble is beginning to rebound near minimum radius. As seen in Fig. 2.9, W_{AC} is not sensitive to the exact endpoint of the collapse. For the numerical integration of Eqn. 2.15, $t = t_n = t(n)$ where $\dot{R}(t_n) < 0$ and $\dot{R}(t_{n+1}) > 0$ suffices.

The significant additional ‘boost’ of energy from the work done by the acoustic wave from R_{max} to collapse is noteworthy in Fig. 2.9. For a $1 \mu\text{m}$ bubble in blood with a 0.5 MPa

acoustic wave, the work done by the acoustic wave on the bubble from $t = 0$ to $t = t_{max}$ where $R_{max} = R(t_{max})$ is 1.74 nJ , while the work done by the acoustic wave on the bubble from $t = t_{max}$ to $t = t_n$ is 51.8 nJ . The total amount of work done by the acoustic wave is then 53.6 nJ , with nearly 97% of that energy coming from the forced collapse phase.

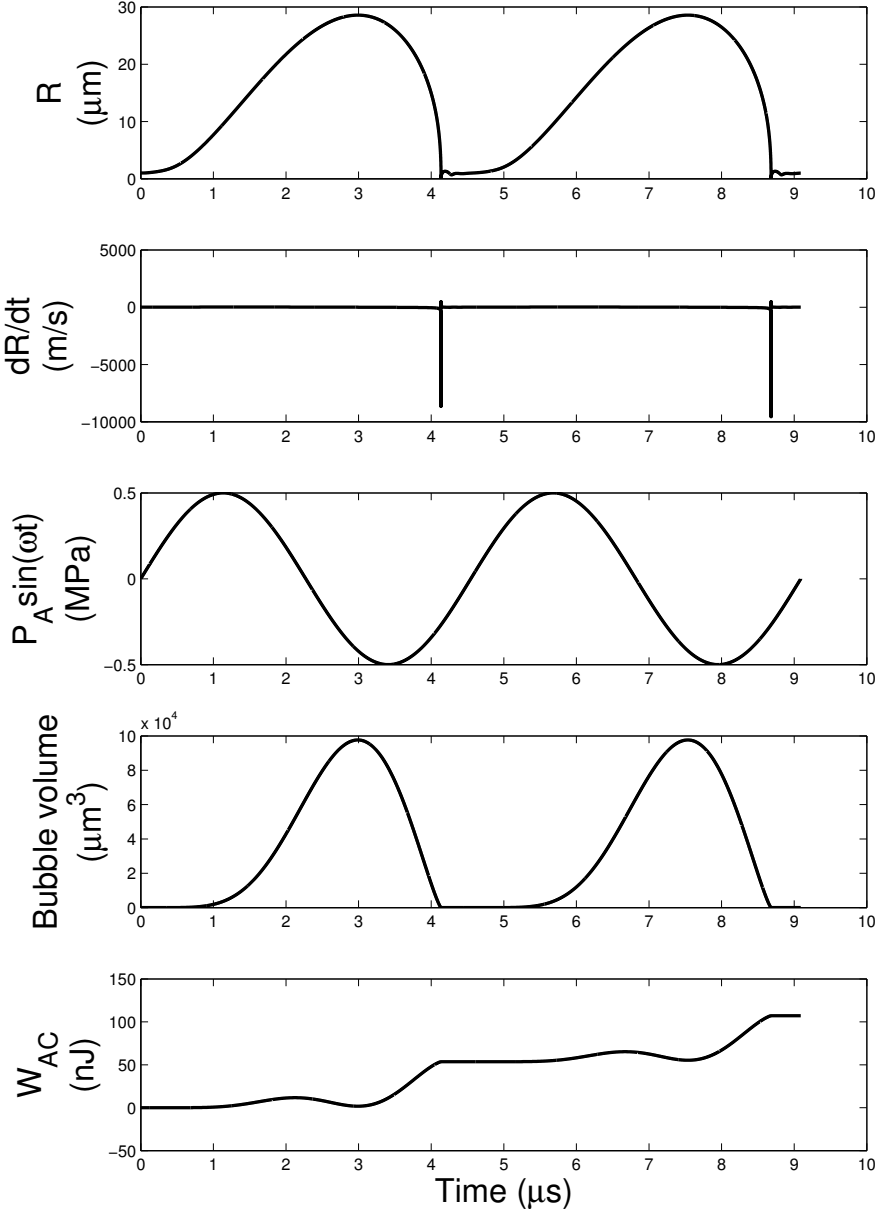


Figure 2.9: A 1 μm bubble in blood subjected to a 0.5 MPa acoustic wave. These plots show the relationship in time between R , \dot{R} , $P_A \sin(\omega t)$, the bubble volume and W_{AC} .

2.4.6 Pressure field design

These methods of estimating the damage can aid in the design of the applied acoustic field. Commercially available ultrasound contrast agents (UCAs) contain a wide distribution of initial microbubble sizes. For example, a commonly used UCA in sonothrombolysis is the UCA from Definity, which contains a distribution of bubbles from less than $1 \mu m$ to $10 \mu m$ in diameter. The majority of the bubbles have a diameter of less than $2 \mu m$ [63, 64]. For a range of initial bubble sizes, the applied acoustic amplitude is varied and energy available to break fibers can be plotted for each of the methods previously described. For example, the maximum amount of damage from an external bubble in blood is shown in Fig. 2.10. As expected, the higher pressure amplitudes lead to larger bubbles and larger potential for damage. There is a resonance around $P_A = 1.5 MPa$ for the smaller sized bubbles. This type of plot can be used to understand better the relationship between the pressure amplitude and the amount of damage to a blood clot.

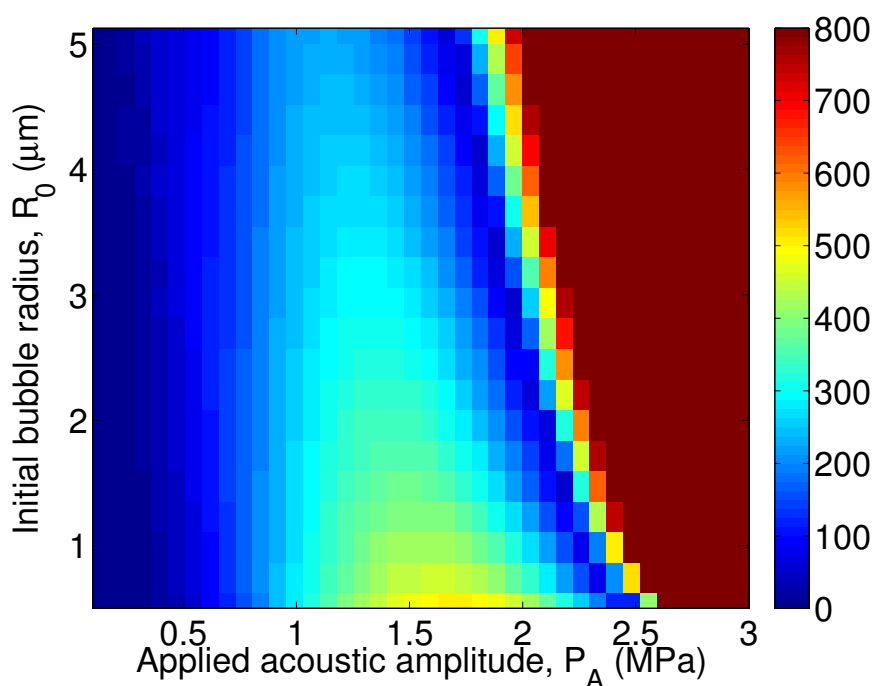


Figure 2.10: The maximum amount of energy available in nJ for breaking fibers from an external bubble is plotted for various initial radii (R_0) and various applied pressure amplitudes (P_A).

2.5 Discussion and Conclusions

In this study, we developed two independent approaches, a strain method and a work-energy based method, for estimating the mechanical damage to a blood clot from a bubble wholly embedded in a clot. The work method was extended to the scenario of a bubble external to the blood clot. The experimental work presented at the beginning of this chapter provides motivation for these estimates, as we try to explain the kind of damage observed. This work is a first step and techniques need to be refined to be able to compare the experiments to the theory.

The first approach to calculate the number of fibers broken is based on the strain of individual fibers as the bubble grows from R_0 to R_{max} . This method indicates that damage is occurring, thus the mechanical properties of the clot are changing. However, the governing equation of the bubble dynamics, Eqns. 2.1-2.3, ignore the destruction of the clot caused by the bubble.

To account for the breaking of fibrin fibers, a modification could be made to the bubble dynamics equation. The addition of this term motivates the second method, an independent work-energy based approach. In this method, the equation for the bubble dynamics, as the bubble grows from R_0 to R_{max} , is analyzed in the form of a work-energy statement. The energy balance for a bubble in a blood clot that does undergo damage is hypothesized here to be similar to that of the energy balance for a bubble in a blood clot that does not undergo damage with an appropriate account of the energy lost to mechanical damage. The notable difference is the addition of a term, energy lost to damage in the clot matrix from fibrin fiber breakage (and red blood cell lysis). This term can be bounded by the limiting cases of a bubble in an undeformed clot and a bubble in blood (a completely destroyed blood clot).

For a bubble wholly embedded in a blood clot, the strain method estimates a smaller amount of damage as compared to the energy method, which provides an upper bound. Thus the two methods are consistent. As the applied acoustic amplitude is increased for both methods, the amount of damage increases. The energy method is more robust and is extended to the scenario of a bubble outside of the blood clot. If the bubble is close enough to the blood clot, it will collapse asymmetrically and create a jet towards the clot. The energy available to break fibers (and lyse blood cells) is bound by the work done on the bubble, from R_0 to collapse, by the acoustic wave. There is significantly more energy available for damage from a bubble growing and collapsing outside the clot compared to a bubble embedded within the clot structure. These results show that at low applied acoustic amplitudes the damage is likely a result of jetting external bubbles but as the amplitude is increased the damage could result from jetting bubbles as well as embedded bubbles.

As seen in Fig. 2.3 right, red blood cells are found in experiments to be lysed during HIFU. The same framework for the energy method, as outlined in this work, can be used to determine the amount of energy available to lyse red blood cells and break fibrin fibers. As red blood cells are lysed and fibrin fibers are broken, the porosity of the clot increases. This may allow for better penetration of microbubbles or thrombolytic drugs. However,

the energy required to lyse a single cell is lacking. This topic will be investigated in future studies.

Chapter 3

Effects of Skull Properties on Cavitation

3.1 Introduction

For the past several decades, ultrasound has been used as a diagnostic modality. More recently, ultrasound has proved as a promising therapeutic tool. High intensity focused ultrasound (HIFU) is an emerging modality for therapeutic ultrasound. Currently, HIFU is in clinical use for treatment of benign prostatic hypertrophy [65] and prostate cancer [66] and in clinical trials for treatment of uterine fibroids [67] and breast cancer [68]. There is ongoing research into the use of HIFU for kidney stone ablation, hemostasis (clot formation), and thrombolysis (clot breakup or dissolution) (see Dalecki [69] and the sources within).

The main mechanism exploited for tumor destruction is thermal necrosis which can occur when part of the wave energy is absorbed by the tissue and converted into heat [70]. However, the mechanisms for sonothrombolysis have been shown to be largely non-thermal [13]. Several studies have shown that acoustic cavitation enhances thrombolytic effects [33, 34, 35]. Cavitation can be induced in the blood stream if the intensity of the acoustic wave is sufficient. Cavitation can be broadly classified into two types, inertial and stable cavitation. Several mechanisms for ultrasound enhanced thrombolysis associated with inertial cavitation (jetting and intense localized stresses) and stable cavitation (micropumping and bubble translation) have been proposed.

Some of the problems associated with the use of HIFU are the attenuation of ultrasound because of the intervening tissue, and the reflection and refraction of the waves as they pass through the heterogeneous tissue en route to the focus [71]. Microbubble cavitation coupled with HIFU therapy enhances sonothrombolysis and has been cited as a solution to the attenuation problem [72], while the use of an array transducer has been suggested as a solution to the focusing problem [73].

The present work contributes to understanding the effects of the physical properties of skull bone when a HIFU wave propagates through it. It also provides a context for using the theory developed in Chapter 2 in a concrete example. The first section of this chapter

deals with the modeling of the HIFU wave propagation through the skull bone focused at a target area within the cranial cavity. In the next section, the dynamical behavior of a test bubble placed at the focus is used to aid in understanding of the pressure field. The pressure variation is a result of the oscillatory nature of HIFU waves. The Keller-Miksis equations is employed to model the radial dynamics of the bubble. Also, the power spectrum of sound emitted when the bubble oscillates is modeled. This allows for a richer understanding of the pressure field.

3.2 HIFU Model

My collaborator, Prashanth Selvaraj, modified a previously published computer model of HIFU tissue ablation [71] to explore the influence of physical properties of compact skull bone on the focusing and attenuation of the HIFU waves. The modifications to the original model used in this work can be found in his master's thesis [74]. The physical dimensions and densities of the skull models used for this study were obtained from a database being collected by our collaborators led by Dr. Thilo Hoelscher at the University of California, San Diego. The skull densities used in this study are 1800 kg/m^3 , 1982 kg/m^3 , and 2164 kg/m^3 for the lower, median, and higher density skull, respectively.

Here, we seek to establish the link between plausible changes in skull properties and consequences for the HIFU field by mimicking the experiment shown in Fig. 3.1. In the *in vitro* experiment, a human cadaver calvaria is immersed in a water bath, with a HIFU transducer arranged outside the skull and a vessel phantom with clot placed (optionally) at the focus.

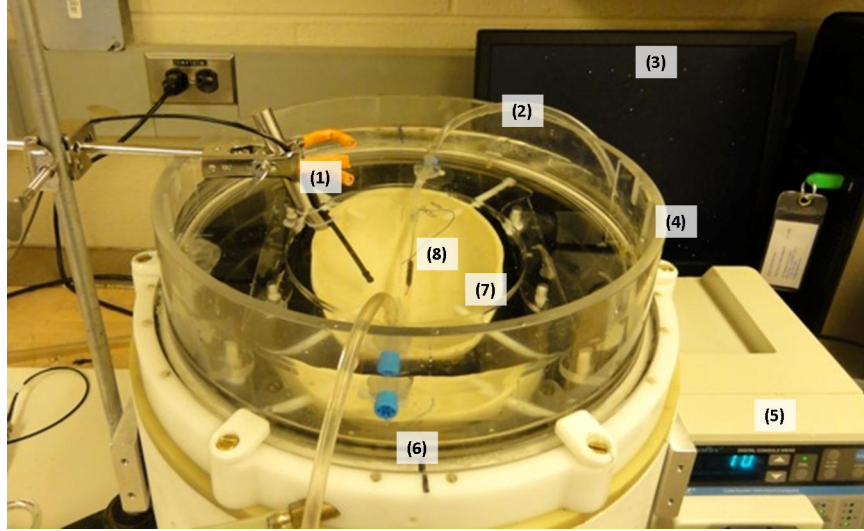


Figure 3.1: Experimental setup: (1) Needle hydrophone for passive cavitation detection system, (2) Flow inlet, (3) Data analysis, (4) Microbubble infusion, (5) Unidirectional flow pump, (6) Hemispherical, helmet transducer filled with deionized, degassed water, (7) Human calvaria mounted on an acrylic fixture, and (8) Human blood clot.

3.3 Cavitation Model

The approach of characterizing a pressure field through the dynamics of a test bubble was used before by our group for shock wave lithotripsy [61]. Moreover, using dynamics of a test bubble to understand the HIFU field makes sense because HIFU-microbubble interactions have been found in prior work to enhance thrombolysis [34, 33, 35].

The plan of this section is as follows. We shall make use of a version of the Keller-Miksis equations due to Yang and Church [38] which is suitable for use in soft tissue. We do this to show a pathway to develop results for *in vivo* modeling, although in the present work - with the *in vitro* experiment of Fig. 3.1 in mind - we set the shear modulus to zero. Next, we consider the sound emitted by a microbubble driven by the HIFU field, in order to make contact with the work of other researchers. Finally, we consider the maximum collapse energy and also the maximum radius to which a test bubble would grow, as this is an indication of the capability of the bubble to deliver mechanical or chemical effects.

3.3.1 Bubble Dynamics

The bubble dynamics are again described by the Keller-Miksis equation with the linear Kelvin-Voigt model for a viscoelastic material, Eqns. 1.1-1.3. The applied acoustic field is $P(t)$, which is found from the HIFU code described below in Sec. 3.2. In the *in vitro*

experiment, shown in Fig. 3.1, the calvaria is fully immersed in water. Therefore we set the physical parameters in Eqns. 1.1-1.3 to $G = 0 Pa$, $\mu = 0.001 kg/m \cdot s$, $P_0 = 1.01 \times 10^5 Pa$, $c = 1484.70 m/s$, $\rho = 998.0 kg/m^3$, $\sigma = 72.8 \times 10^{-3} N/m$ and $\kappa = 1.4$.

3.3.2 Sound Emission

The sound emitted from the bubble oscillation has been used to characterize the type of cavitation [39]. The acoustic pressure radiated by the bubble is given by

$$P_s(t) = \rho \frac{R}{r} \left(\ddot{R}R + 2\dot{R}^2 \right) \quad (3.1)$$

where R is the bubble radius at time t and r is the distance from the center of the bubble. The Fast Fourier Transform (FFT) of this data is used to determine the frequency content of the signal, which has been used as an indication of the type of cavitation present. The presence of harmonics and subharmonics of the driving frequency is indicative of stable cavitation, while an increase in the broadband noise arises from inertial cavitation.

3.3.3 Connection to Mechanical Damage

Using the method developed in Section 2.4.5 for a bubble outside of a blood clot, the maximum energy available to break fibers and red blood cells can be found. The work done on the bubble from the acoustic wave as the bubble radius changes from $R(t_1)$ at time t_1 to $R(t_2)$ at time t_2 is

$$W_{AC} = -4\pi \int_{t_1}^{t_2} P_\infty R^2 \dot{R} dt. \quad (3.2)$$

The bubble is undergoing a forced collapse, therefore the work done by the acoustic wave on the bubble is calculated through the expansion and collapse. Therefore, an upper bound on the number of fibers broken can be estimated by assuming all of the work done on the bubble until collapse by the acoustic wave is transferred to the clot, which is then available to break fibers and red blood cells.

3.4 Results

3.4.1 Pressure Distribution

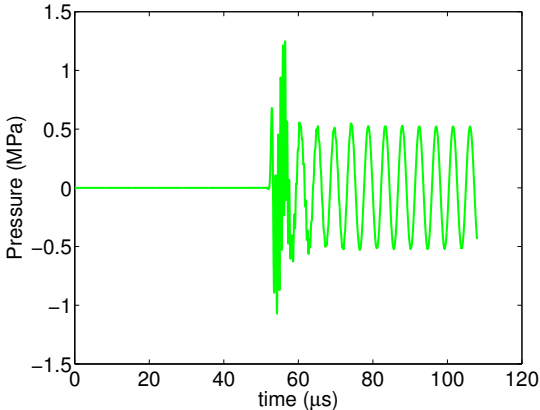
The HIFU model uses the basic equations for ultrasound propagation through an inhomogeneous medium. This leads to the displacement of the focal point away from the geometrical focus. By assigning a phase delay to individual transducers in the array a sharper focus can

be obtained, and the focal point of the waves and the geometrical focus of the array can be made to coincide. The results without focusing, that is without applying a phase delay, can be found in [74]. From this work, we find that as the density of the model calvaria increases, the pressure contours become less sharp. There is also a decrease in the absolute values of the peak positive and negative pressures within the computational domain, and in particular near the focus.

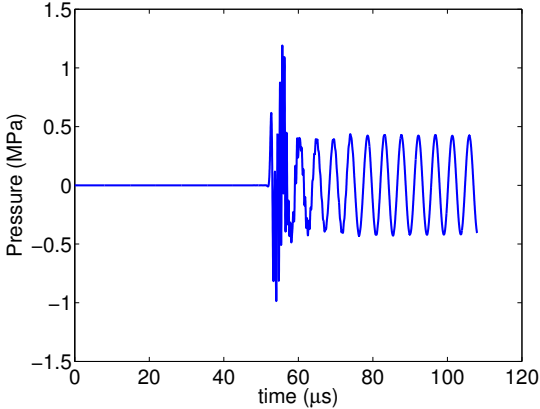
The pressure variation due to the change in density of the skull model used is evident at the focus, see Fig. 3.2. The leading spikes in the plot at a time of around $58 \mu s$ are due to the transducers being switched on and off instantaneously in our model. Physically, this is not possible; a transducer would require a finite amount of time to reach peak output. However, this spike in pressure is stabilized within 5 or 6 μs , and propagates towards the perfectly matched layer at the boundaries where it is absorbed. Therefore, the spike is neglected when measuring peak positive and peak negative pressure, see Table 3.1, and when calculating the dynamics of a test bubble, to which we now turn.

	Peak Positive Pressure (<i>MPa</i>)	Peak Negative Pressure (<i>MPa</i>)
Lower density skull	0.557	0.628
Median density skull	0.436	0.486
Higher density skull	0.352	0.394

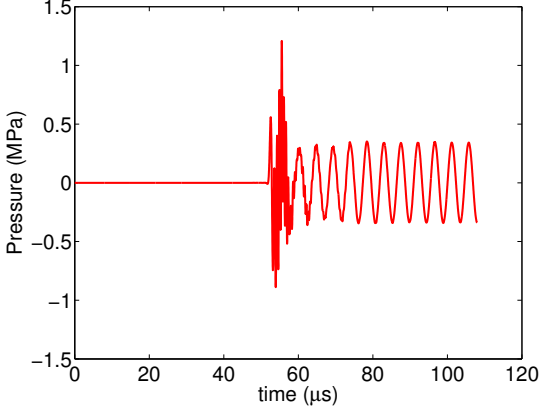
Table 3.1: Peak positive and peak negative pressure at the focus for median density, lower density and higher density skulls.



(a) Lower density skull



(b) Median density skull



(c) Higher density skull

Figure 3.2: Temporal variation of the pressure at the focus for a lower, median and higher density skulls.

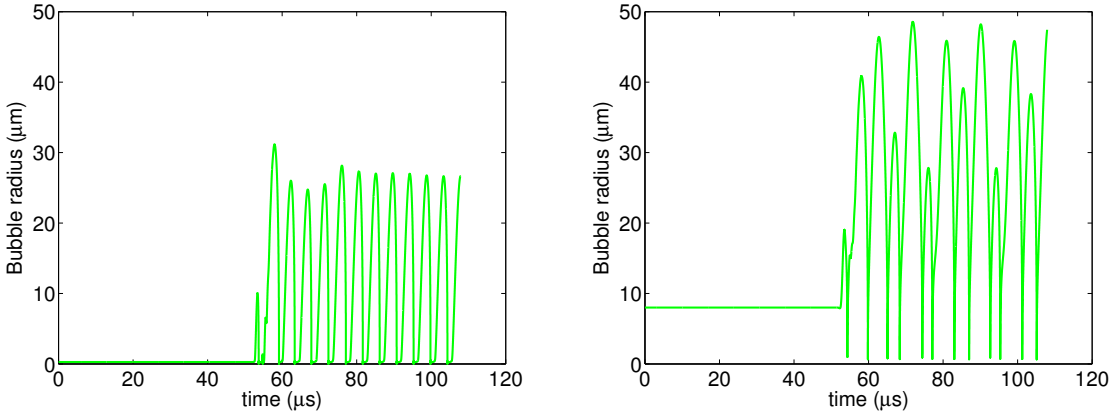
3.4.2 Effects of Skull Density on Dynamics of a Test Bubble

The effect of the HIFU wave on the dynamics of the test bubble is depicted in Fig. 3.3 for bubbles with initial radii of $0.27 \mu\text{m}$ and $8.0 \mu\text{m}$ respectively. The $0.27 \mu\text{m}$ bubble is chosen to demonstrate the onset of cavitation as the density of the skull is varied, while the $8.0 \mu\text{m}$ bubble is chosen to show the transition from stable to inertial cavitation for bubbles subject to the same pressure waves passing through skull models of different densities.

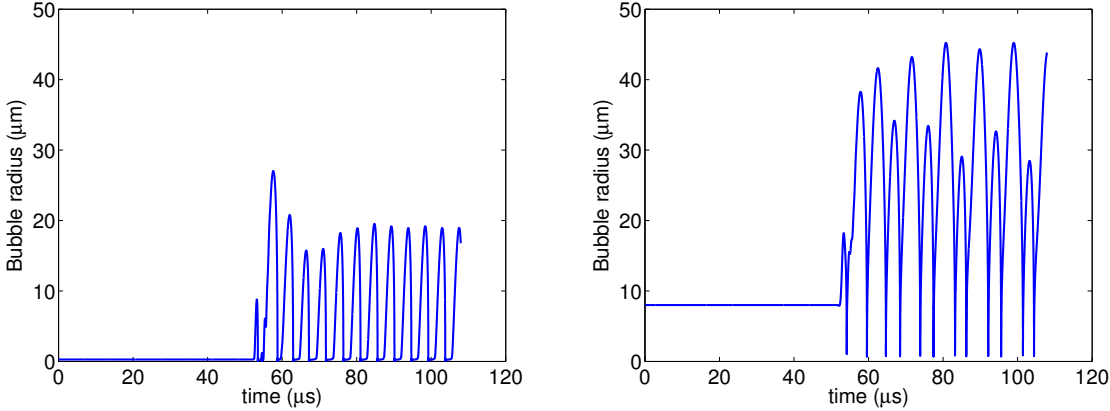
The pressure variation at the focus is higher for the models with the lower density skulls, and hence the bubble shows a more dramatic response in terms of radial growth. With the skull of lower density in place, the test bubble grows from a radius of $0.27 \mu\text{m}$ to a maximum instantaneous radius of $28.2 \mu\text{m}$, while the model with the skull of median density produces a bubble with a maximum instantaneous radius of $20.8 \mu\text{m}$. Again, the leading spike in bubble radius is a result of the spike in pressure values, which in turn is caused by the instantaneous switching of the transducer from a dormant to an active state. This is to be neglected.

It is interesting to note that the initial radius of the bubble affects the dynamics of radial growth. The minimum bubble radius above which the HIFU waves have an effect on the bubble is called the point of cavitation inception [39]. This threshold radius is around $0.27 \mu\text{m}$ for the model with the denser skull, as shown in left column of Fig. 3.3.

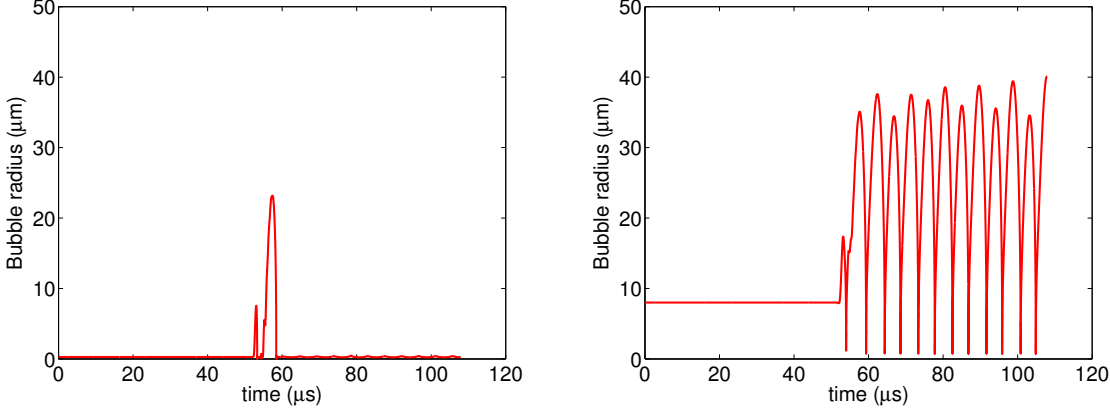
When a bubble of larger radius located at the focus is studied, a very different bubble growth pattern is seen. The right column of Fig. 3.3 depicts a bubble of radius $8.0 \mu\text{m}$ at the focus. While the maximum radius attained by the bubble is consistent with results from smaller bubbles, the minimum bubble radius falls well below the initial radius. The sharp collapse and subsequent rebound of the bubble radius is indicative of having passed the inertial cavitation threshold, which is defined as the point at which cavitation changes from a stable to an inertially dominated state. Also, in the case with the median density skull, subharmonic or period doubled radial oscillations is observed, see Fig. 3.3b right. The period doubling route to chaos has been shown under certain conditions to transform a single frequency spectrum into a broad band noise spectrum [75]. However, we shall examine the acoustic power spectrum of the test bubble in the next section to obtain a clearer picture of the nature of cavitation being induced by the HIFU waves.



(a) Lower density skull



(b) Median density skull



(c) Higher density skull

Figure 3.3: Radial dynamics of a bubble in water with initial radius of $0.27 \mu m$ in the left column and $8.0 \mu m$ in the right column located at the focus for a lower, median and higher density skulls.

3.4.3 Power Spectrum of Emitted Sound

The power spectrum of the sound emitted by a bubble can be used to classify the type of cavitation present. It is obtained by taking the Fast Fourier Transform (FFT) of the sound produced by the oscillating bubble given by Eqn. 3.1. The FFT is an efficient algorithm used to compute the Discrete Fourier Transform, which decomposes a discrete signal into its constituent frequencies.

The finite length of the sound signal can lead to approximation errors. As we increase the sampling rate of the signal, we obtain a better approximation to the continuous signal. Therefore, increasing the sampling rate will produce better approximations on average. We numerically increase the sampling, N , until the FFT amplitude converges to determine an appropriate sampling rate to take, see Fig. 3.4.

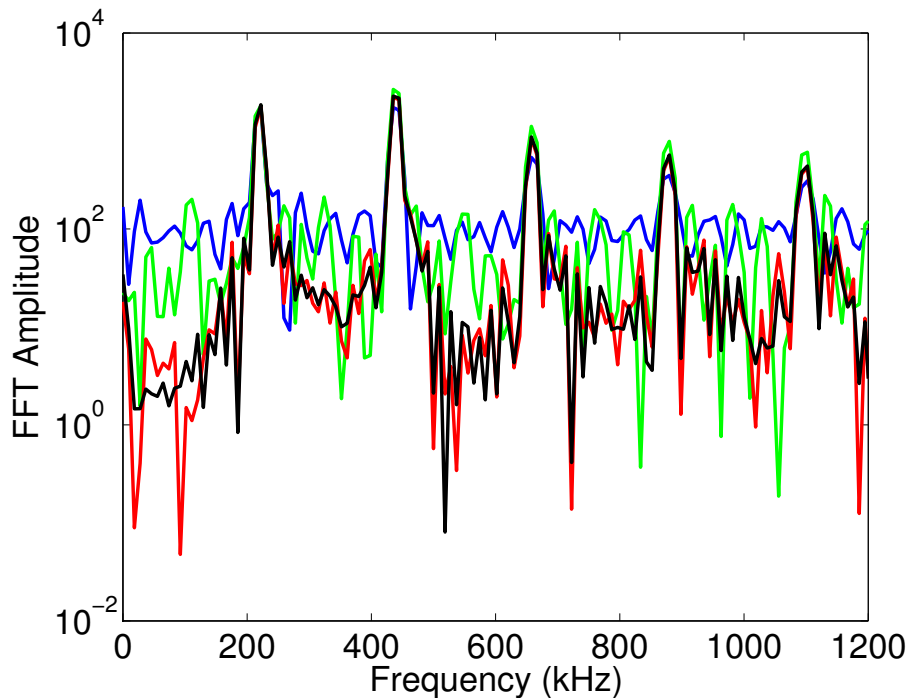


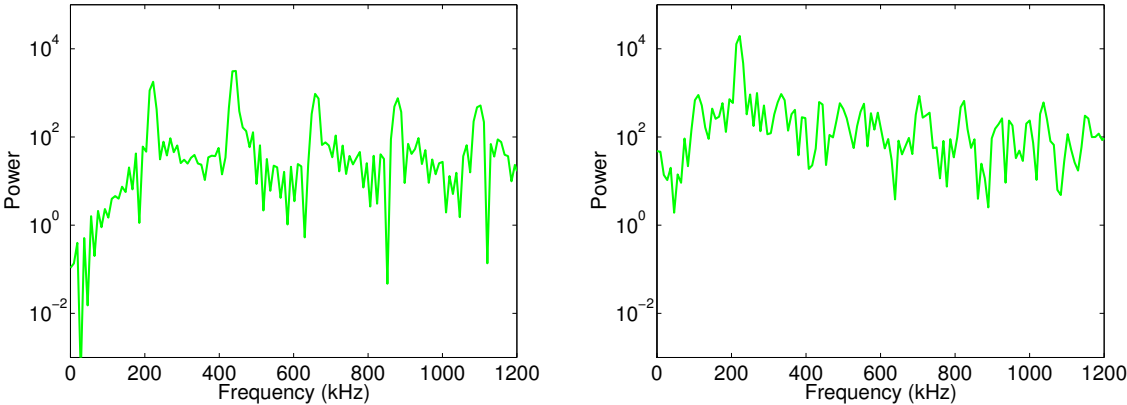
Figure 3.4: Convergence of the power spectrum for a bubble in water with initial radius of $1 \mu\text{m}$ for $(-)$ $N = 10^3$, $(-)$ $N = 10^4$, $(-)$ $N = 10^5$, and $(-)$ $N = 10^6$. As the length, N , of the sound signal is increased, the resolution of the FFT increases. Suitable convergence is found.

A spectrum with peaks at harmonic and sub-harmonic frequencies of the driving frequency is indicative of stable cavitation, while a broadband spectrum is indicative of inertial cavitation [35]. Of course, a distinct categorization of a power spectrum as being indicative of either inertial or stable cavitation is not possible as there is a continuum of behavior in between. However, the power spectrum does offer a useful view into how a bubble of an

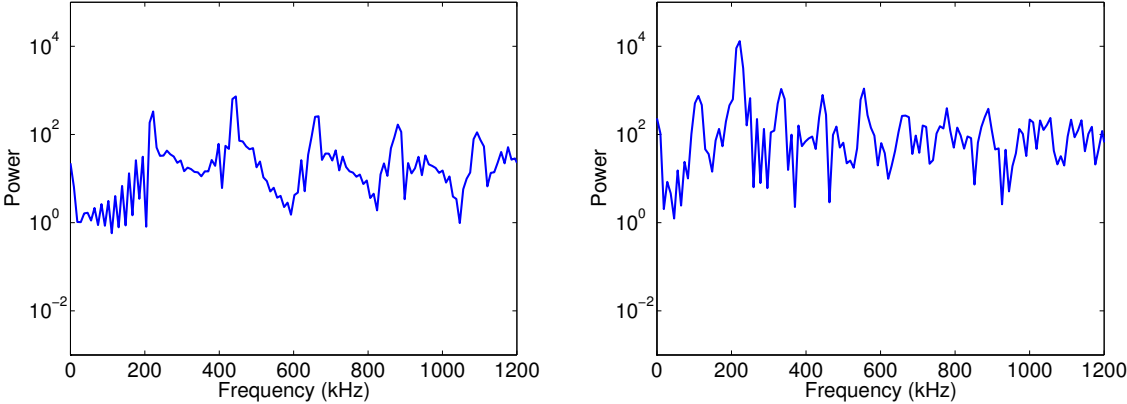
initial radius behaves when subjected to HIFU waves of a certain frequency and amplitude. Also, the power spectrum is easily obtained experimentally, for an example of experimentally obtained data see Sec. 2.3.2. Therefore, we compute the FFT for the test bubble at the focus as a way to connect with experimental work. Plots of the power spectrum for bubbles with radii of $0.27 \mu m$ and $8.0 \mu m$ are shown in Fig. 3.5.

In Fig. 3.5c left, the sound emitted by the $0.27 \mu m$ test bubble with the denser calvaria is almost negligible, and so no sharp peaks can be seen. This is an indication of the HIFU field not having substantial effect on the bubble, as can be seen in the plot of the modest radial growth in Fig. 3.3c left. The power spectra for the model with the lower and median density calvaria in Figs. 3.5a & 3.5b left, however, shows peaks at the driving frequency and its harmonics, which is indicative of stable cavitation.

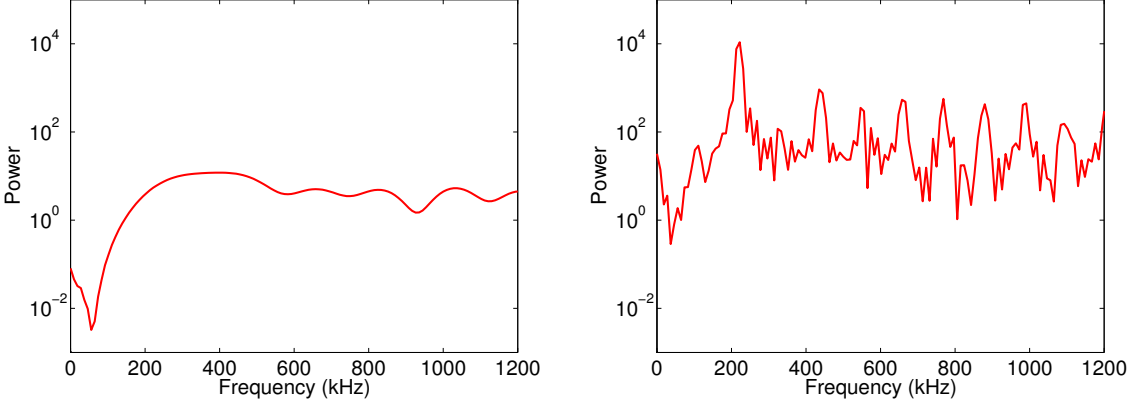
The power spectra for a $8.0 \mu m$ bubble at the focus, show a marked change in behavior from the spectra of the $0.27 \mu m$ bubble. Firstly, the total power emitted has increased by a couple of orders of magnitude. For the lower density skull test case (Fig. 3.5c right), a slight increase in the broadband spectrum indicative of inertial cavitation is seen. There is a sharp peak in the power spectrum at the driving frequency and the harmonics. As the density of the skull model is decreased to the median skull density, peaks in the power spectrum are also seen at the harmonics and subharmonic ($f/2$) of the driving frequency. In Fig. 3.5b right, harmonics and subharmonics are more distinct at lower frequencies pointing to stable cavitation, while a diminished broadband spectrum at higher frequencies indicates a mix of stable and inertial cavitation over the whole range of frequencies. In Fig. 3.5a right, the only distinguishable peak is at the driving frequency, but the elevation of the broadband spectrum at higher frequencies indicates a change to inertial cavitation.



(a) Lower density skull



(b) Median density skull



(c) Higher density skull

Figure 3.5: Acoustic power spectrum of a bubble in water with an initial radius of $0.27 \mu m$ in the left column and $8.0 \mu m$ in the right column located at the focus for a lower, median and higher density skulls.

3.4.4 Connection to Mechanical Damage

To demonstrate how the pressure field affects bubble dynamics at various points in the domain, the plots of R_{max}/R_0 for a bubble of various initial radii along the x -, y -, and z -axes are shown in Fig. 3.6 left for the lower density skull, in Fig. 3.7 left for the median density skull, and in Fig. 3.8 left for the higher density skull. The focal point is the origin in each plot. The y -axis is parallel to the line connecting the center of the transducer array to the geometrical focal point. The phased array, and therefore the pressure field, is nearly axisymmetric about the y -axis (i.e. in the xz -plane). This leads to nearly identical R_{max} plots along x - and z - axes, see Figs. 3.6a & 3.6c left, 3.7a & 3.7c left, and 3.8a & 3.8c left. The maximum bubble radius decreases as the density of the calvaria increases, reaffirming the conclusion that HIFU waves have a weaker effect on bubble dynamics at lower pressures.

Finally, Figs. 3.6b left, 3.7b left, and 3.8b left show the variation of the maximum bubble radius on either side of the focus along the y -axis. The geometrical symmetry of the array transducer around the y -axis leads to a sharp focus in the xz -plane. In the yz - or xy - planes, focusing is done using time reversal techniques where each transducer element is assigned a phase delay. This work deals with unfocused HIFU waves, resulting in a more gradual change of pressure around the focus along the y -axis, as opposed to sharper variations seen along the x - and z - axes.

The changes in the pressure field, due to the the variation in skull density, affect the potential for a microjetting bubble outside of the blood clot to cause mechanical damage. For each applied acoustic signal, the maximum amount of energy available to break clot material for a single bubble collapse is calculated for various initial radii. Eqn. 3.2 is calculated such that the bubble expansion and collapse contains the largest maximum bubble radius, R_{max} . Mathematically, $t_1 < t_{max} < t_2$ where $R_{max} = R(t_{max})$, t_1 is when the bubble starts to grow, and t_2 is the collapse.

The maximum amount of energy available to break fibers for various initial radii along the x -, y -, and z - axes are shown in Fig. 3.6 right for the lower density skull, in Fig. 3.7 right for the median density skull, and in Fig. 3.7 right for the higher density skull. For each axis, the plots of the energy are similar in shape for each skull density. The initial radii with the highest energy area increases slightly as the density of the skull is increased. The contour limits in the lower and higher density skull are +50% and -25%, respectively, of the limits in the median skull. This shows that as the pressure amplitude of the HIFU wave is increased there is more potential for jetting to cause mechanical damage to the blood clot.

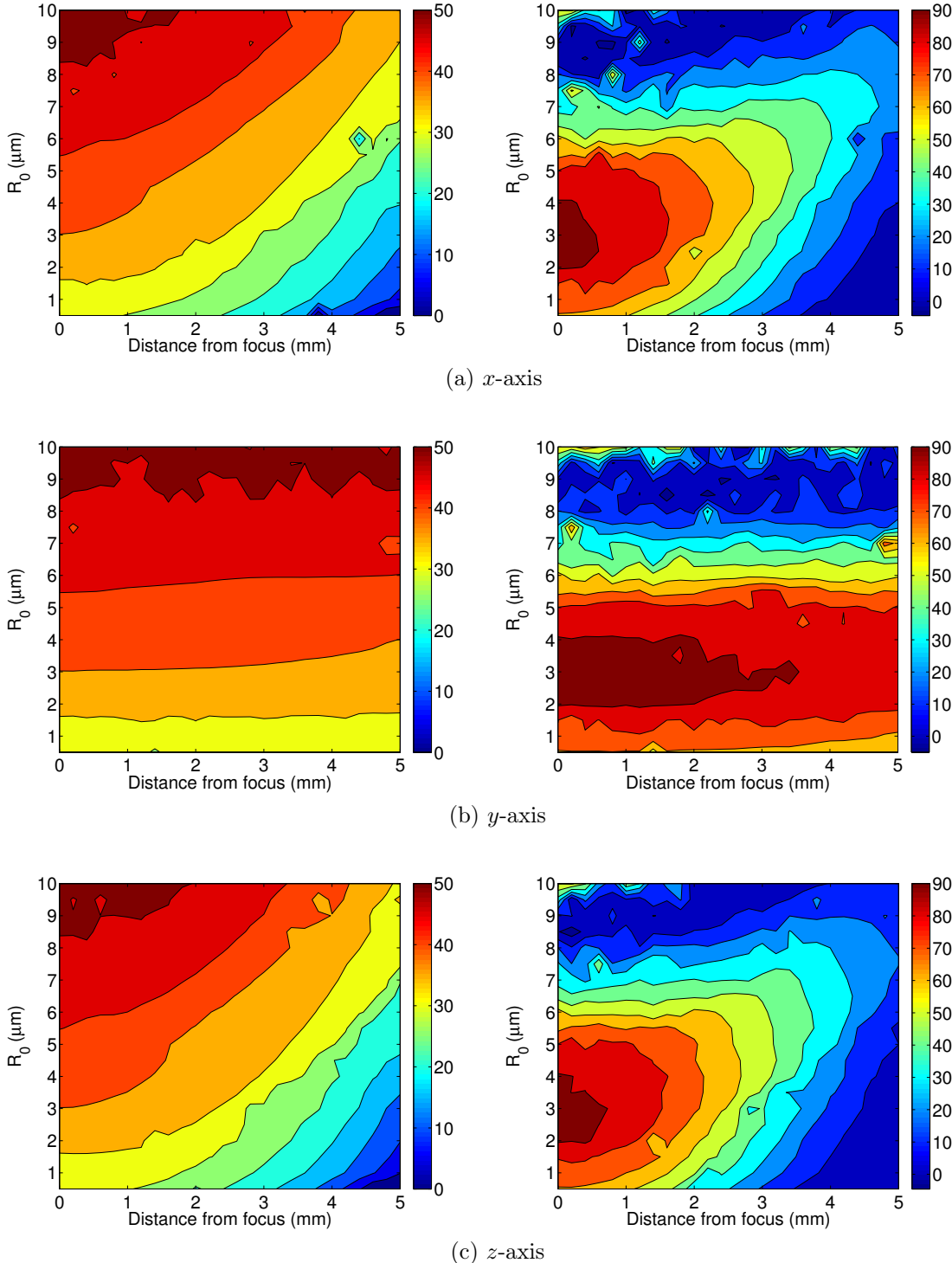


Figure 3.6: The maximum radii in μm (left) and amount of energy available to break fibers and red blood cells in nJ (right) along each axis as the initial bubble radius is varied for a calvaria of LOWER density. The focus is located at 0 mm on each axis.

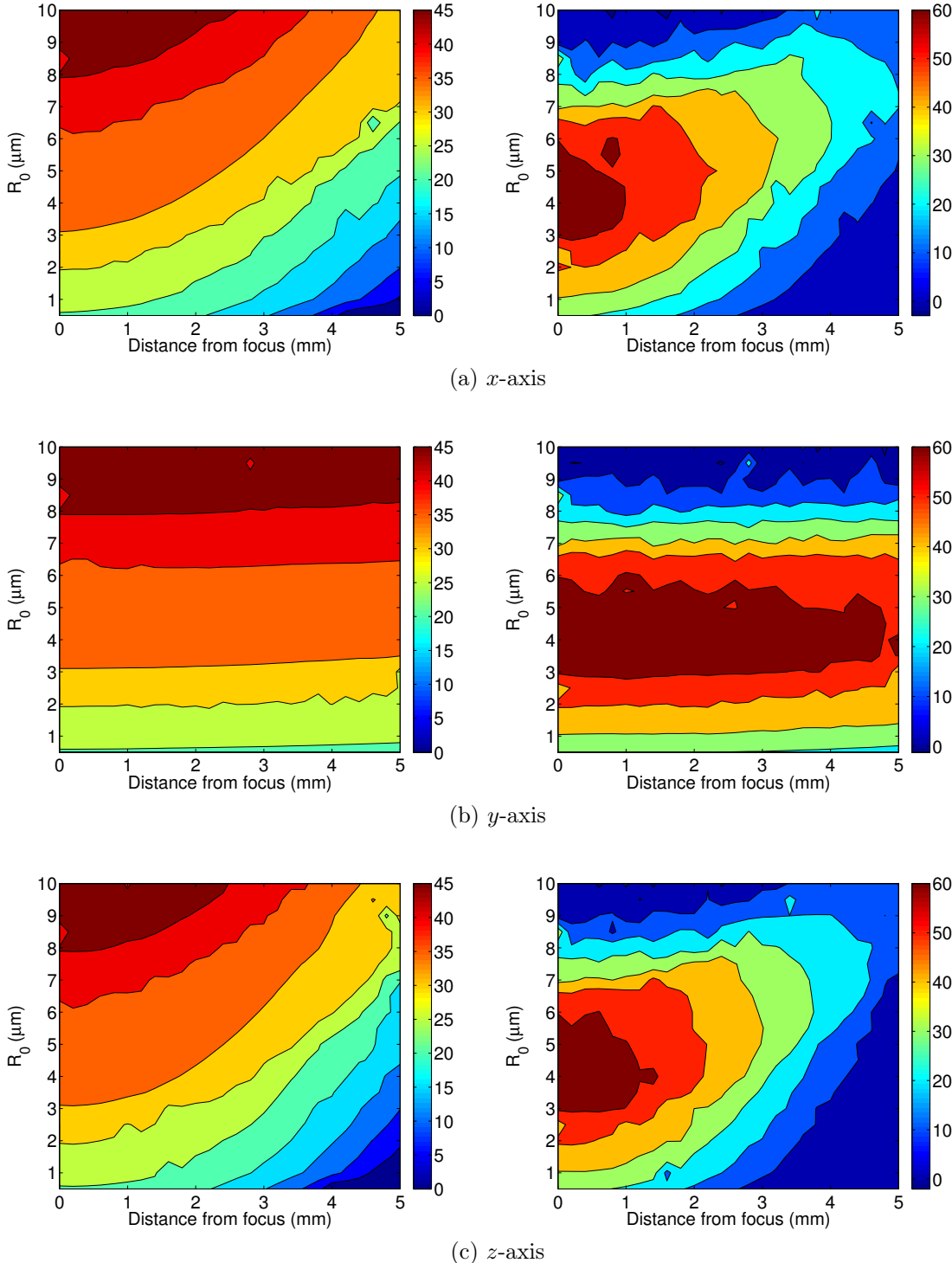


Figure 3.7: The maximum radii in μm (left) and amount of energy available to break fibers and red bloods cells in nJ (right) along each axis as the initial bubble radius is varied for a calvaria of MEDIAN density. The focus is located at 0 mm on each axis.

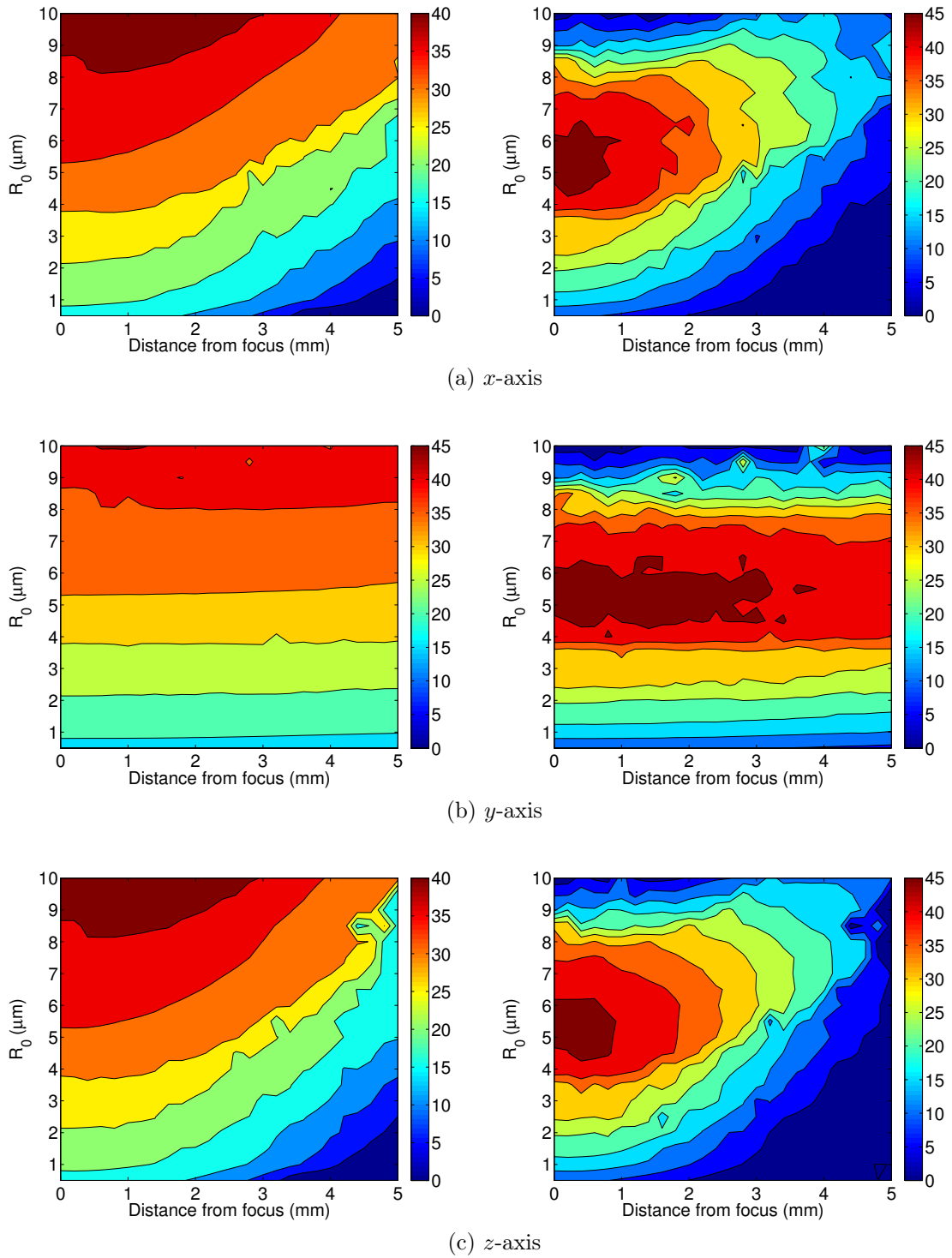


Figure 3.8: The maximum radii in μm (left) and amount of energy available to break fibers and red blood cells in nJ (right) along each axis as the initial bubble radius is varied for a calvaria of HIGHER density. The focus is located at 0 mm on each axis.

3.5 Conclusion

The effect of the density of compact skull bone on the propagation of HIFU waves through the cranial cavity has been studied [74], as an example of how one can apply the theory of Chapter 2. This was simulated with a fully three dimensional time resolved numerical method. As a direct consequence of the varying pressure field in the domain, a test bubble placed at the focus undergoes cavitation that can be described as stable (at one end of a continuous range) or inertial (at the other end), or somewhere in between. The dynamics of a test bubble are useful to aid in the interpretation of the HIFU field, as it is altered by calvaria of different physical properties. Cavitation *in vivo* is of course much more complicated.

There is a strong effect on the pressure at the focus, for calvaria of different densities. For the same wave produced by the phased array, the pressure amplitude at the focus of the wave increases as the density of the calvaria the wave passes through decreases. Future work should examine the influence of the diploe, a spongy layer of trabecular bone and inclusions filled with blood or soft tissue, and the layered architecture of the skull cross-section, to determine the influence on HIFU focusing and attenuation.

There is a threshold initial radius at which the HIFU wave has an effect on the dynamics of the test bubble and the acoustic power spectrum of emitted sound. The maximum radius a bubble will grow to also varies according to the density of the calvaria. As an example to demonstrate mechanical damage as a viable mechanism for clot destruction, the scenario of a test bubble, of various initial radii, outside of the blood clot was examined. The maximum amount of energy available to cause damage to a blood clot increases as the density of the calvaria decreases.

Finally, as initial bubble radius increases, there is a shift from stable to inertial cavitation, and this is evident in the acoustic power spectrum as well as the bubble dynamics. There is usually a mixture of both stable and inertial cavitation present.

Chapter 4

Discussion

Cavitation is important in sonothrombolysis in combination with thrombolytic agents and without. To further the efficiency of these methods, the cavitation mechanisms need to be determined. Currently, researchers only suggest potential cavitation mechanisms but no one has gone as far as to examine individual mechanisms and their role during thrombolysis. Experiments suggest that stable cavitation plays a more important role than inertial cavitation in ultrasound mediated thrombolysis with rt-PA and microbubbles. The type of cavitation present during sonothrombolysis with microbubbles and no fibrinolytic drugs still needs to be investigated.

4.1 Summary of contributions

This work is a first step into identifying plausible mechanisms by which cavitation enhances sonothrombolysis. The Keller-Miksis equation with linear Kelvin-Voigt material, developed by Yang and Church [38], is used to model the dynamics of a single bubble embedded in a blood clot, and for a single bubble in the near vicinity of a blood clot. This bubble dynamics model is common to the two otherwise independent approaches we derived to estimate the mechanical cavitation damage to a blood clot. The high intensity focused ultrasound (HIFU) field is approximated by a sinusoidal wave with varying pressure amplitude and fixed frequency. The motivation for these approaches comes from experimental data.

The first method examined the stretch of individual fibrin fibers as a bubble in an isotropic, viscoelastic material, with mean properties of the blood clot, expands to its maximum radius during HIFU insonation. The motion is affine and the fibrin fibers of the blood clot's structure are stretched as the bubble expands. The initial orientation of fibers is random. A mapping of the fiber's length and orientation is made from the initial configuration to the deformed configuration at the bubble's maximum radius. In the deformed configuration, each fiber's stretch is known based on its initial orientation from the radial direction. Experimental data gives a maximum strain for fibrin fibers of 147%, beyond which the fibers

will rupture. This critical strain, easily converted to a critical stretch, is converted to a critical azimuthal angle from the radial in the initial configuration. The total number of broken fibers, in a spherically symmetric region, can then be summed in the initial configuration. The analytical expression for the total number of broken fibers cannot be solved, so a brute force calculation is made. The number of fibers is then converted to the total amount of energy used to break that many fibers, as the energy to break a single fiber is known.

This first method assumes that no damage is occurring to the blood clot structure as the bubble expands to its maximum radius, while it suggests that fibrin fibers are breaking during the expansion. To account for the damage occurring to the clot, a modification could be made to the bubble dynamical equations. This provides the motivation for the second approach to estimating the damage from an expanding embedded bubble. Adding a term to the Keller-Miksis equation is equivalent to added a term to the work-energy statement for the system. This new term, the energy lost to damage in the clot matrix from fibrin fiber breakage and red blood cell lysis, is bounded by quantities from the limiting scenarios of a bubble in an undamaged clot and a bubble in a completely damage clot (blood). This method provides an upper bound on the amount of energy available to do damage to the blood clot. Comparing these two independent methods, we find that they are consistent.

The energy method is extended to the case of a bubble external to a blood clot. The bubble grows nearly symmetrically, as in the case of an embedded bubble, but now as it is not constrained by the clot material, the bubble grows to a much larger size. A bubble close enough to the clot will collapse asymmetrically and a jet will form directed at the clot. The amount of kinetic energy in the jet is related to the amount of work done by the acoustic wave on the bubble from growth until collapse. The kinetic energy of the jet is then available to break fibrin fibers and lyse red blood cells, providing an upper bound on the amount of energy available to cause damage to the blood clot. This method estimates that external bubbles have the potential to cause more damage to a blood clot than bubbles embedded in the clot structure. This work also demonstrated that at low applied acoustic amplitudes the mechanical damage is likely a result of jetting bubbles but as the amplitude is increased the damage could result from jetting bubbles and embedded bubbles.

Next, we explored the effects of the physical properties of skull bone when a HIFU wave propagates through it, as an example for application of the theory. As the density of compact skull bone is increased, the amplitude of the pressure at the focus decreases, for the same wave produced by the phased array. To aid in understanding the pressure field, the dynamics of a test bubble are analyzed. The power spectrum of sound emitted when the bubble oscillates is examined and used to understand the type of cavitation (stable and/or inertial). The amount of mechanical damage from a test bubble is calculated for a bubble in water (to mimic a specific experimental setup) external to a blood clot. Various initial radii are examined. We demonstrated that the maximum amount of energy available to cause damage to a blood clot increases as the density of the calvaria decreases.

In summary, the goal of this work was to explore the plausibility of mechanical damage as a means by which microbubbles and cavitation appear to enhance thrombolysis in a HIFU

field. Such a mechanism indeed seems plausible, based on the work presented here, but further investigation is necessary to develop a deeper understanding.

4.2 Future work

While this work has provided some initial clues into mechanical cavitation damage, there is still much work to be done. Techniques need to be refined to be able to compare the experimental work to the theoretical work. Development of an experimental assay of damage is underway with our collaborators, Thilo Hoelscher's group, at the University of California, San Diego. Our goal is to be able to compare directly the experimental data on the extent of damage to a blood clot from a cavitating bubble and the results of the theoretical and numerical estimates developed in this dissertation.

The two methods derived in this work to estimate the amount of damage from a bubble can be improved. First, a simple improvement to the methods would be to use blood clot material properties from a relevant frequency regime. However, this data is unavailable at this time. In the future, should this data become available, they only need be incorporated into the bubble model and methods described in this dissertation (i.e. the methods formed here are still valid). As seen from experimental data (Fig. 2.3 right) there is cellular matrix that has been released due to cell lysis. The same framework for the energy method, as outlined in this work, can be used to determine the amount of energy available to lyse red blood cells and break fibrin fibers. Similarly, the strain method could incorporate the critical rupture stretch of a red blood cell. However, the energy required to lyse a single cell and the rupture strain is lacking. Also, the bounds on $W_{AC,D}$, the energy available to do damage for a blood clot undergoing damage, can be refined. Here for the external bubble, we use the spherical collapse as an upper bound to the actual asymmetrical collapse. Further work needs to be done to look at details of the forced asymmetrical collapse. Also, the energy transfer from the asymmetrical collapse to the jet and from the jet to the clot material should be investigated, in the future.

Other cavitation mechanisms need to be investigated. Several studies suggest that stable cavitation is important during ultrasound enhanced thrombolysis with rt-PA and microbubbles [34, 35, 20]. The suggested mechanism is micropumping, with this aiding the penetration of the thrombolytic drugs deeper into the clot matrix. An important experimental parameter of the blood clot for this mechanism is clot porosity. Currently, the data available on clot porosity is limited to fibrin clots without the red blood cells and platelets entrapped. New experimental data is needed on whole human blood clots. Also, the different mechanisms employed to enhance thrombolysis may be working together to break apart the blood clot. As mechanical damage occurs (lysing of red blood cells and fibrin fibers breaking), the porosity of the clot increases. In this situation, micropumping, which allows for better penetration of microbubbles or thrombolytic drugs, may play an even more important role than on its own.

Our analysis of the role of physical skull properties on the pressure field and bubble dynamics suggests some areas for future projects, as well. The effect of changes in the skull properties on the cavitation threshold could be studied. With more simulated and/or experimental pressure data, the effects of varying skull properties on the amount of energy available for damage can be assessed. Eventually, this work can be compared with experimental data for greater insight.

Bibliography

- [1] Centers for Disease Control and Prevention. Types of stroke. http://www.cdc.gov/stroke/types_of_stroke.htm, July 2012.
- [2] World Health Organization. The top 10 causes of death. <http://www.who.int/mediacentre/factsheets/fs310/en/index.html>, July 2012.
- [3] Writing Group Members, V. L. Roger, A. S. Go, D. M. Lloyd-Jones, E. J. Benjamin, J. D. Berry, W. B. Borden, D. M. Bravata, S. Dai, E. S. Ford, C. S. Fox, H. J. Fullerton, C. Gillespie, S. M. Hailpern, J. A. Heit, V. J. Howard, B. M. Kissela, S. J. Kittner, D. T. Lackland, J. H. Lichtman, L. D. Lisabeth, D. M. Makuc, G. M. Marcus, A. Marelli, D. B. Matchar, C. S. Moy, D. Mozaffarian, M. E. Mussolino, G. Nichol, N. P. Paynter, E. Z. Soliman, P. D. Sorlie, N. Sotoodehnia, T. N. Turan, S. S. Virani, N. D. Wong, D. Woo, and M. B. Turner. Heart disease and stroke statistics 2012 update. *Circulation*, 125(1):e2–e220, 2012.
- [4] R. Kothari, L. Sauerbeck, E. Jauch, J. Broderick, T. Brott, J. Khoury, and T. Liu. Patients’ awareness of stroke signs, symptoms, and risk factors. *Stroke*, 28(10):1871–1875, 1997.
- [5] K. Das, G. P. Mondal, A. K. Dutta, B. Mukherjee, and B. B. Mukherjee. Awareness of warning symptoms and risk factors of stroke in the general population and in survivors stroke. *Journal of Clinical Neuroscience*, 14(1):12 – 16, 2007.
- [6] S. Sug Yoon, R. F. Heller, C. Levi, J. Wiggers, and P. E. Fitzgerald. Knowledge of stroke risk factors, warning symptoms, and treatment among an australian urban population. *Stroke*, 32(8):1926–1930, 2001.
- [7] A. Hickey, A. O’Hanlon, H. McGee, C. Donnellan, E. Shelley, F. Horgan, and D. O’Neill. Stroke awareness in the general population: knowledge of stroke risk factors and warning signs in older adults. *BMC Geriatrics*, 9:35, 2009.
- [8] K. J. Greenlund, L. J. Neff, Z. J. Zheng, N. L. Keenan, W. H. Giles, C. A. Ayala, J. B. Croft, and G. A. Mensah. Low public recognition of major stroke symptoms. *American Journal of Preventive Medicine*, 25(4):315 – 319, 2003.

- [9] G. J. del Zoppo, J. L. Saver, E. C. Jauch, and H. P. Adams. Expansion of the time window for treatment of acute ischemic stroke with intravenous tissue plasminogen activator. *Stroke*, 40(8):2945–2948, Aug 2009.
- [10] I. L. Katzan, M. D. Hammer, E. D. Hixson, A. J. Furlan, A. Abou-Chebl, and D. M. Nadzam. Utilization of intravenous tissue plasminogen activator for acute ischemic stroke. *Archives of Neurology*, 61(3):346–350, 2004.
- [11] D. Kleindorfer, B. Kissela, A. Schneider, D. Woo, J. Houry, R. Miller, K. Alwell, J. Gebel, J. Szafarski, A. Pancioli, E. Jauch, C. Moomaw, R. Shukla, and J. P. Broderick. Eligibility for recombinant tissue plasminogen activator in acute ischemic stroke. *Stroke*, 35(2):e27–29, Feb 2004.
- [12] C. G. Lauer, R. Burge, D. B. Tang, B. G. Bass, E. R. Gomez, and B. M. Alving. Effect of ultrasound on tissue-type plasminogen activator-induced thrombolysis. *Circulation*, 86(4):1257–1264, 1992.
- [13] C. W. Francis, P. T. Onundarson, E. L. Carstensen, A. Blinc, R. S. Meltzer, K. Schwarz, and V. J. Marder. Enhancement of fibrinolysis *in vitro* by ultrasound. *Journal of Clinical Investigation*, 90(5):2063–2068, Nov 1992.
- [14] A. Blinc, C. W. Francis, J. L. Trudnowski, and E. L. Carstensen. Characterization of ultrasound-potentiated fibrinolysis *in vitro*. *Blood*, 81(10):2636–2643, 1993.
- [15] K. Tachibana and S. Tachibana. Albumin microbubble echo-contrast material as an enhancer for ultrasound accelerated thrombolysis. *Circulation*, 92(5):1148–1150, Sep 1995.
- [16] T. R. Porter, R. F. LeVeen, R. Fox, A. Kricsfeld, and F. Xie. Thrombolytic enhancement with perfluorocarbon-exposed sonicated dextrose albumin microbubbles. *American Heart Journal*, 132(5):964–968, Nov 1996.
- [17] S. Westermark, H. Wiksell, H. Elmqvist, K. Hultenby, and H. Berglund. Effect of externally applied focused acoustic energy on clot disruption *in vitro*. *Clinical Science*, 97(1):67–71, 1999.
- [18] V. Frenkel, J. Oberoi, M. J. Stone, M. Park, C. Deng, B. J. Wood, Z. Neeman, M. Horne, and K. C. Li. Pulsed high-intensity focused ultrasound enhances thrombolysis in an *in vitro* model. *Radiology*, 239(1):86–93, April 2006.
- [19] U. Rosenschein, V. Furman, E. Kerner, I. Fabian, J. Bernheim, and Y. Eshel. Ultrasound imaging guided noninvasive ultrasound thrombolysis: Preclinical results. *Circulation*, 102(2):238–245, 2000.

- [20] C. K. Holland, S. S. Vaidya, S. Datta, C. C. Coussios, and G. J. Shaw. Ultrasound-enhanced tissue plasminogen activator thrombolysis in an *in vitro* porcine clot model. *Thrombosis Research*, 121(5):663 – 673, 2008.
- [21] T. Hoelscher, D. Fisher, R. Raman, K. Ernstrom, E. Zadicario, W. G. Bradley, and A. Voie. Noninvasive transcranial clot lysis using high intensity focused ultrasound. *Journal of Neurology and Neurophysiology*, S1, 2011.
- [22] A Kashyap, A Blinc, V. J. Marder, D. P. Penney, and C. W. Francis. Acceleration of fibrinolysis by ultrasound in a rabbit ear model of small vessel injury. *Thrombosis Research*, 76(5):475–485, 1994.
- [23] R. Kornowski, R. S. Meltzer, A. Chernine, Z. Vered, and A. Battler. Does external ultrasound accelerate thrombolysis? results from a rabbit model. *Circulation*, 89(1):339–344, 1994.
- [24] Y. Birnbaum, H. Luo, T. Nagai, M. C. Fishbein, T. M. Peterson, S. Li, D. Kricsfeld, T. R. Porter, and R. J. Siegel. Noninvasive *in vivo* clot dissolution without a thrombolytic drug: recanalization of thrombosed iliofemoral arteries by transcutaneous ultrasound combined with intravenous infusion of microbubbles. *Circulation*, 97(2):130–134, Jan 1998.
- [25] V. N. Suchkova, R. B. Baggs, and C. W. Francis. Effect of 40-khz ultrasound on acute thrombotic ischemia in a rabbit femoral artery thrombosis model : Enhancement of thrombolysis and improvement in capillary muscle perfusion. *Circulation*, 101(19):2296–2301, 2000.
- [26] J. Eggers, B. Koch, K. Meyer, I. Konig, and G. Seidel. Effect of ultrasound on thrombolysis of middle cerebral artery occlusion. *Annals of Neurology*, 53(6):797–800, 2003.
- [27] A. V. Alexandrov, A. M. Demchuk, W. S. Burgin, D. J. Robinson, and J. C. Grotta. Ultrasound-enhanced thrombolysis for acute ischemic stroke: Phase i. findings of the clotbust trial. *Journal of Neuroimaging*, 14(2):113–117, 2004.
- [28] A. V. Alexandrov, C. A. Molina, J. C. Grotta, Z. Garami, S. R. Ford, J. Alvarez-Sabin, J. Montaner, M. Saqqur, A. M. Demchuk, L. A. Moyé, M. D. Hill, and A. W. Wojner. Ultrasound-enhanced systemic thrombolysis for acute ischemic stroke. *New England Journal of Medicine*, 351(21):2170–2178, 2004.
- [29] W. C. Culp, T. R. Porter, J. Lowery, F. Xie, P. K. Roberson, and L. Marky. Intracranial clot lysis with intravenous microbubbles and transcranial ultrasound in swine. *Stroke*, 35(10):2407–2411, Oct 2004.

- [30] J. Eggers, G. Seidel, B. Koch, and I. R. König. Sonothrombolysis in acute ischemic stroke for patients ineligible for rt-pa. *Neurology*, 64(6):1052–1054, 2005.
- [31] F. Xie, J. M. Tsutsui, J. Lof, E. C. Unger, J. Johannig, W. C. Culp, T. Matsunaga, and T. R. Porter. Effectiveness of lipid microbubbles and ultrasound in declotting thrombosis. *Ultrasound in Medicine & Biology*, 31(7):979–985, Jul 2005.
- [32] M. J. Stone, V. Frenkel, S. Dromi, P. Thomas, R. P. Lewis, K. C. Li, M. Horne, and B. J. Wood. Pulsed-high intensity focused ultrasound enhanced tpa mediated thrombolysis in a novel *in vivo* clot model, a pilot study. *Thrombosis Research*, 121(2):193–202, 2007.
- [33] E. C. Everbach and C. W. Francis. Cavitation mechanisms in ultrasound-accelerated thrombolysis at 1 mhz. *Ultrasound in Medicine & Biology*, 26(7):1153–1160, September 2000.
- [34] S. Datta, C. C. Coussios, L. E. McAdory, J. Tan, T. Porter, G. De Courten-Myers, and C. K. Holland. Correlation of cavitation with ultrasound enhancement of thrombolysis. *Ultrasound in Medicine & Biology*, 32(8):1257–1267, August 2006.
- [35] A. F. Prokop, A. Soltani, and R. A. Roy. Cavitation mechanisms in ultrasound-accelerated fibrinolysis. *Ultrasound in Medicine & Biology*, 33(6):924–933, 2007.
- [36] J. Slikkerveer, G. Veen, Y. Appelman, N. van Royen, and O. Kamp. Therapeutic application of ultrasound: contrast-enhanced thrombolysis in acute ST-elevation myocardial infarction; the Sonolysis study. *Netherlands Heart Journal*, 19(4):200–205, Apr 2011.
- [37] D. W. Newell, M. M. Shah, R. Wilcox, D. R. Hansmann, E. Melnychuk, J. Muschelli, and D. F. Hanley. Minimally invasive evacuation of spontaneous intracerebral hemorrhage using sonothrombolysis. *Journal of Neurosurgery*, 115(3):592–601, Sep 2011.
- [38] X. Yang and C.C. Church. A model for the dynamics of gas bubbles in soft tissue. *Journal of the Acoustical Society of America*, 118(6):3595–3606, 2005.
- [39] T. G. Leighton. *The Acoustic Bubble*. Academic Press, 1997.
- [40] V. L. Roger, A. S. Go, D. M. Lloyd-Jones, R. J. Adams, J. D. Berry, T. M. Brown, M. R. Carnethon, S. Dai, G. de Simone, E. S. Ford, C. S. Fox, H. J. Fullerton, C. Gillespie, K. J. Greenlund, S. M. Hailpern, J. A. Heit, P. M. Ho, V. J. Howard, B. M. Kissela, S. J. Kittner, D. T. Lackland, J. H. Lichtman, L. D. Lisabeth, D. M. Makuc, G. M. Marcus, A. Marelli, D. B. Matchar, M. M. McDermott, J. B. Meigs, C. S. Moy, D. Mozaffarian, M. E. Mussolino, G. Nichol, N. P. Paynter, W. D. Rosamond, P. D. Sorlie, R. S. Stafford, T. N. Turan, M. B. Turner, N. D. Wong, and J. Wylie-Rosett. Heart disease and stroke statistics - 2011 update: A report from the american heart association. *Circulation*, 123(4):e18–209, 2011.

- [41] A. Barreto. Intravenous thrombolytics for ischemic stroke. *Neurotherapeutics*, 8:388–399, 2011. 10.1007/s13311-011-0049-x.
- [42] J. W. Weisel. The mechanical properties of fibrin for basic scientists and clinicians. *Biophysical Chemistry*, 112(2-3):267–276, 2004. John D. Ferry Special Issue.
- [43] J. P. Collet, H. Shuman, R. E. Ledger, S. Lee, and J. W. Weisel. The elasticity of an individual fibrin fiber in a clot. *Proceedings of the National Academy of Sciences*, 102(26):9133–9137, 2005.
- [44] E. A. Ryan, L. F. Mockros, J. W. Weisel, and L. Lorand. Structural origins of fibrin clot rheology. *Biophysical Journal*, 77(5):2813–2826, Nov 1999.
- [45] W. Liu, L. M. Jawerth, E. A. Sparks, M. R. Falvo, R. R. Hantgan, R. Superfine, S. T. Lord, and M. Guthold. Fibrin fibers have extraordinary extensibility and elasticity. *Science*, 313(5787):634, 2006.
- [46] W. Liu, C. R. Carlisle, E. A. Sparks, and M. Guthold. The mechanical properties of single fibrin fibers. *Journal of Thrombosis and Haemostasis*, 8(5):1030–1036, May 2010.
- [47] C. R. Carlisle, C. Coulais, M. Namboothiry, D. L. Carroll, R. R. Hantgan, and M. Guthold. The mechanical properties of individual, electrospun fibrinogen fibers. *Biomaterials*, 30(6):1205–1213, 2009.
- [48] C. R. Carlisle, E. A. Sparks, C. Der Loughian, and M. Guthold. Strength and failure of fibrin fiber branchpoints. *Journal of Thrombosis and Haemostasis*, 8(5):1135–1138, 2010.
- [49] W. W. Roberts, O. Kramer, R. W. Rosser, F. H. Nestler, and J. D. Ferry. Rheology of fibrin clots. i. : Dynamic viscoelastic properties and fluid permeation. *Biophysical Chemistry*, 1(3):152–160, 1974.
- [50] C Gerth, W. W. Roberts, and J. D. Ferry. Rheology of fibrin clots ii : Linear viscoelastic behavior in shear creep. *Biophysical Chemistry*, 2(3):208–217, 1974.
- [51] C. C. Huang, C. C. Shih, T. Y. Liu, and P. Y. Lee. Assessing the viscoelastic properties of thrombus using a solid-sphere-based instantaneous force approach. *Ultrasound in Medicine & Biology*, 37(10):1722–1733, October 2011.
- [52] F. G. Mitri and Z. E. Fellah. Instantaneous axial force of a high-order bessel vortex beam of acoustic waves incident upon a rigid movable sphere. *Ultrasonics*, 51(6):719–724, Aug 2011.
- [53] P Riha, X. Wang, R. Liao, and J. F. Stoltz. Elasticity and fracture strain of whole blood clots. *Clinical Hemorheology & Microcirculation*, 21(1):45–49, 1999.

- [54] J. B. Keller and M. Miksis. Bubble oscillations of large amplitude. *Journal of the Acoustical Society of America*, 68(2):628–633, 1980.
- [55] K. C. Gersh, K. E. Edmondson, and J. W. Weisel. Flow rate and fibrin fiber alignment. *Journal of Thrombosis and Haemostasis*, 8(12):2826–2828, 2010.
- [56] A. E. Brown, R. I. Litvinov, D. E. Discher, P. K. Purohit, and J. W. Weisel. Multiscale mechanics of fibrin polymer: Gel stretching with protein unfolding and loss of water. *Science*, 325(5941):741–744, 2009.
- [57] A. J. Szeri and L. G. Leal. A new computational method for the solution of flow problems of microstructured fluids. part 1. theory. *Journal of Fluid Mechanics*, 242:549–576, 1992.
- [58] R. B. Bird, R. C. Armstrong, and O. Hassager. *Dynamics of Polymeric Liquids*, volume 1: Fluid Dynamics. John Wiley & Sons, Inc., 2 edition, 1987.
- [59] M. L. Calvisi, J. I. Iloreta, and A. J. Szeri. Dynamics of bubbles near a rigid surface subjected to a lithotripter shock wave. part 2. reflected shock intensifies non-spherical cavitation collapse. *Journal of Fluid Mechanics*, 616:63–97, 2008.
- [60] A. Pearson, J. R. Blake, and S. R. Otto. Jets in bubbles. *Journal of Engineering Mathematics*, 48:391–412, 2004. 10.1023/B:engi.0000018172.53498.a2.
- [61] J. I. Iloreta, Y. Zhou, G. N. Sankin, P. Zhong, and A. J. Szeri. Assessment of shock wave lithotripters via cavitation potential. *Physics of Fluids*, 19(8):086103, aug 2007.
- [62] M. L. Calvisi, O. Lindau, J. R. Blake, and A. J. Szeri. Shape stability and violent collapse of microbubbles in acoustic traveling waves. *Physics of Fluids*, 19(4):047101, 2007.
- [63] D. E. Goertz, N. de Jong, and van der Steen A. F.W. Attenuation and size distribution measurements of Definity and manipulated Definity populations. *Ultrasound in Medicine & Biology*, 33(9):1376 – 1388, 2007.
- [64] S. Stapleton, H. Goodman, Y. Zhou, E. Cherin, R. M. Henkelman, P. N. Burns, and F. S. Foster. Acoustic and kinetic behaviour of Definity in mice exposed to high frequency ultrasound. *Ultrasound in Medicine & Biology*, 35(2):296 – 307, 2009.
- [65] N. T. Sanghvi, R. S. Foster, R. Bihrlé, R. Casey, T. Uchida, M. H. Phillips, J. Syrus, A. V. Zaitsev, K. W. Marich, and F. J. Fry. Noninvasive surgery of prostate tissue by high intensity focused ultrasound: an updated report. *European Journal of Ultrasound*, 9(1):19–29, 1999.

- [66] A. Gelet, J. Y. Chapelon, R. Bouvier, O. Rouviere, Y. Lasne, D. Lyonnet, and J. M. Dubernard. Transrectal high-intensity focused ultrasound: minimally invasive therapy of localized prostate cancer. *Journal of Endourology*, 14(6):519–528, Aug 2000.
- [67] E. A. Stewart, J. Rabinovici, C. M. Tempany, Y. Inbar, L. Regan, B. Gastout, G. Hesley, H. S. Kim, S. Hengst, and W. M. Gedroyc. Clinical outcomes of focused ultrasound surgery for the treatment of uterine fibroids. *Fertility and Sterility*, 85(1):22–29, Jan 2006.
- [68] F. Wu, Z. B. Wang, Y. D. Cao, W. Z. Chen, J. Bai, J. Z. Zou, and H. Zhu. A randomised clinical trial of high-intensity focused ultrasound ablation for the treatment of patients with localised breast cancer. *British Journal of Cancer*, 89(12):2227–2233, Dec 2003.
- [69] D. Dalecki. Mechanical bioeffects of ultrasound. *Annual Review of Biomedical Engineering*, 6:229–248, 2004.
- [70] G. T. Haar and C. Coussios. High intensity focused ultrasound: physical principles and devices. *International Journal of Hyperthermia*, 23(2):89–104, Mar 2007.
- [71] K. Okita, S. Takagi, K. Ono, and Y. Matsumoto. Development of high intensity focused ultrasound simulator for large-scale computing. *International Journal of Numerical Methods Fluids*, 65(1-3):43–66, 2011.
- [72] C. C. Coussios and R. A. Roy. Applications of acoustics and cavitation to noninvasive therapy and drug delivery. *Annual Review of Fluid Mechanics*, 40(1):395–420, 2008.
- [73] T. Hoelscher, W. G. Wilkening, S. Molkenstruck, H. Voit, and C. Koch. Transcranial sound field characterization. *Ultrasound in Medicine & Biology*, 34(6):973–980, 2008.
- [74] P. Selvaraj. Use of high intensity focused ultrasound (hifu) for transcranial sonothrombolysis. Master’s thesis, Ecole Polytechnique, 2011.
- [75] W. Lauterborn and E. Cramer. Subharmonic route to chaos observed in acoustics. *Physical Review Letters*, 47:1445–1448, Nov 1981.

Appendix A

Geometric derivation for strain

For a spherical bubble surrounded by an incompressible fluid undergoing an oscillation with the following set of evolution equations

$$\begin{aligned} r(t) &= (r_0^3 + R(t)^3 - R_0^3)^{1/3} \\ \theta(t) &= \theta_0 \\ \phi(t) &= \phi_0, \end{aligned}$$

the principal stretches are

$$\begin{aligned} \lambda_1 &= r_0^2 (r_0^3 + R(t)^3 - R_0^3)^{-2/3} \\ \lambda_2 = \lambda_3 &= \frac{1}{r_0} (r_0^3 + R(t)^3 - R_0^3)^{1/3}. \end{aligned}$$

The principal stretches were derived using tensor notation. The principal stretches can be related to the engineering strain e_i by $e_i = \lambda_i - 1$, giving

$$\begin{aligned} e_1 &= r_0^2 (r_0^3 + R(t)^3 - R_0^3)^{-2/3} - 1 \\ e_2 = e_3 &= \frac{1}{r_0} (r_0^3 + R(t)^3 - R_0^3)^{1/3} - 1. \end{aligned}$$

Alternatively, and as a check, the maximum engineering strain can be found using a geometric derivation. The maximum strain in the θ and ϕ directions is

$$e_{max,\theta} = \frac{L_{max} - L_0}{L_0} = \frac{(r_0^3 + R_{max}^3 - R_0^3)^{1/3} - r_0}{r_0}$$

where $L_0 = 2\pi r_0 \delta\alpha$, $L_{max} = 2\pi r_{max} \delta\alpha$ and $\delta\alpha$ is the subtended angle of the arcs L_0 and L_{max} in the θ or ϕ directions. For the radial direction, the maximum engineering strain is

$$e_{max,r} = \frac{\delta r_{max} - \delta r_0}{\delta r_0}$$

where δr_0 is the thickness of a shell in the undeformed configuration which is deformed to a shell of thickness δr_{max} at t_{max} (where $R_{max} = R(t_{max})$). The volume of the shell remains constant and therefore

$$\begin{aligned}\delta r_{max} &= \left((r_0 + \delta r_0)^3 + r_{max}^3 - r_0^3 \right)^{1/3} - r_{max} \\ &= \left((r_0 + \delta r_0)^3 + R_{max}^3 - R_0^3 \right)^{1/3} - \left(r_0^3 + R_{max}^3 - R_0^3 \right)^{1/3}.\end{aligned}$$

Expanding for small δr_0 (and $r_0^2 \delta r_0$ small) we have

$$\begin{aligned}\delta r_{max} &= \left(r_0^3 + 3r_0^2 \delta r_0 + 3r_0 \delta r_0^2 + \delta r_0^3 + R_{max}^3 - R_0^3 \right)^{1/3} - \left(r_0^3 + R_{max}^3 - R_0^3 \right)^{1/3} \\ &\approx \left(r_0^3 + R_{max}^3 - R_0^3 + 3r_0^2 \delta r_0 \right)^{1/3} - \left(r_0^3 + R_{max}^3 - R_0^3 \right)^{1/3} \\ &\approx \left(r_0^3 + R_{max}^3 - R_0^3 \right)^{1/3} + 3r_0^2 \delta r_0 \cdot \frac{1}{3} \left(r_0^3 + R_{max}^3 - R_0^3 \right)^{-2/3} + O(\delta r_0^2) - \left(r_0^3 + R_{max}^3 - R_0^3 \right)^{1/3} \\ &\approx r_0^2 \delta r_0 \left(r_0^3 + R_{max}^3 - R_0^3 \right)^{-2/3}\end{aligned}$$

To leading order, the maximum strain in the radial direction is

$$e_{max,r} = \frac{r_0^2 \delta r_0 \left(r_0^3 + R_{max}^3 - R_0^3 \right)^{-2/3} - \delta r_0}{\delta r_0} = r_0^2 \left(r_0^3 + R_{max}^3 - R_0^3 \right)^{-2/3} - 1$$

The two derivations (tensor-based and geometrical) provide the same results.